Automated extraction of water bodies from NIR and RGB aerial imagery in northern Alaska using supervised and unsupervised machine learning techniques

---

Author:
Ahmed Abdelwahab

Supervisors:
Prof.Dr. Guido Grosse
Dr. Ingmar Nitze

A thesis submitted in fulfillment
of the requirements for the degree of
Master of Science

Department of Remote Sensing, geoInformation and Visualization
Campus Golm
Faculty of Earth Sciences

Universität Potsdam

ALFRED-WEGENER-INSTITUT
HELMHOLTZ-ZENTRUM FÜR POLAR- UND MEERESFORSCHUNG

Potsdam University
Potsdam, Germany

March 2021-2022

Automated extraction of water bodies from NIR and RGB aerial imagery in northern Alaska using supervised and unsupervised machine learning techniques, © March 2021-2022

Author:
Ahmed Abdelwahab

Supervisors:
Prof.Dr. Guido Grosse
Dr. Ingmar Nitze

Institute:
Potsdam University, Potsdam, Germany

CONTENTS

LIST OF FIGURES

LIST OF TABLES

ABSTRACT

Thawing and freezing of permafrost ground are affected by various reasons: air temperature, vegetation, snow accumulation, subsurface physical properties, and moisture. Due to the rising of air temperature, the permafrost temperature and the thermokarst activity increase. Thermokarst instability causes an imbalance for the hydrology system, topography, soils, sediment and nutrient cycle to lakes and streams. Hence the lakes and ponds are ubiquitous in permafrost region. The plants and animals fulfil their nutrient needs from water in the environment. Other animals acquire their needs from the plants and animals that they consume. Therefore the influence of degradation of lakes and ponds strongly affect biogeochemical cycles.

This research aims to implement an automated workflow to map the water bodies caused by permafrost thawing. The scientific challenge is to test the machine learning techniques adaptability to assist the observation and mapping of the water bodies using aerial imagery. The study area is mainly located in northern Alaska and consists of five different locations: Ikpikpuk, Teschekpuk Central, Teshekpuk East, Tesheckpuk West, Meade East, and Meade West. To estimate the degradation of the high centred polygons distribution and potential degradation of ice wedges, I mapped the polygonal terrain and ice-wedge melt ponds using areal photogrammetry data of NIR and RGB bands captured by Thaw Trend Air 2019 flight campaign.

The techniques used are unsupervised K-mean classification, supervised segment mean shift, and supervised random forest classification to model the water polygons from airborne photogrammetry. There are two phases to perform the machine learning classification; the first step is to test the accuracy of each technique and get to a conclusion about the most adapted method. The second is to prepare the Orthomosaic data, run the chosen workflow, and visualize the final results. The morphology filter with opening option application and clean boundary filters are practical before classification as they sharpen the image features. The conclusion is to use the Random forest classification as it was helpful in all NIR Orthomosaics; however, the RGB images required downsampling to provide adequate accuracy.

ZUSAMMENFASSUNG

Das Auftauen und Gefrieren von Permafrostböden wird durch verschiedene Faktoren beeinflusst: Lufttemperatur, Vegetation, Schneeansammlung, physikalische Eigenschaften des Untergrunds und Feuchtigkeit. Durch den Anstieg der Lufttemperatur erhöht sich die Permafrosttemperatur und die Thermokarst Aktivität. Die Instabilität im Thermokarst führt zu einem Ungleichgewicht des hydrologischen Systems, der Topographie, der Böden sowie des Sediment- und Nährstoffkreislaufs in Seen und Flüssen. Daher sind Seen und Teiche in Permafrostgebieten allgegenwärtig. Die Pflanzen und Tiere decken ihren Nährstoffbedarf aus dem Wasser in der Umwelt. Andere Tiere beziehen ihren Bedarf aus den Pflanzen und Tieren die sie verzehren. Daher wirkt sich der Einfluss der Degradation von Seen und Teichen stark stark auf die biogeochemischen Kreisläufe aus. Ziel dieser Forschung ist die Einführung eines automatisierten Arbeitsablaufs zur Kartierung von Gewässern, die durch das Auftauen des Permafrostes entstehen. Die wissenschaftliche Herausforderung besteht darin, die Anpassungsfähigkeit der Techniken des maschinellen Lernens zu testen, um die Beobachtung und Kartierung von Gewässern anhand von Luftbildern zu unterstützen.

Das Untersuchungsgebiet befindet sich hauptsächlich im Norden Alaskas und besteht aus fünf verschiedenen Orten: Ikpikpuk, Teschekpuk Central, Teshekpuk East, Teshekpuk West, Meade East, und Meade West. Um die Degradation der hochzentrierten Polygone und die potenzielle Degradation der Eiskeile abzuschätzen, habe ich das polygonale Gelände und die Schmelztümpel der Eiskeile mit Hilfe flächenhafter Photogrammetriedaten der NIR- und RGB-Bänder kariert. Die Photogrammetriedaten wurden während der Thaw Trend Air 2019 Flugkampagne aufgenommen wurden.

Die verwendeten Techniken sind unbeaufsichtigte K-Mittelwert-Klassifizierung, überwachte Segment-Mittelwertverschiebung und überwachte Random-Forest-Klassifizierung zur Modellierung der Wasserpolygone aus der Luft. Die Klassifizierung mit maschinellem Lernen erfolgt in zwei Phasen; im ersten Schritt wird die Genauigkeit der einzelnen Verfahren getestet, um zu einer Entscheidung über die am besten geeignete Methode zu gelangen. Im zweiten Schritt werden die Orthomosaikdaten vorbereitet, der gewählte Arbeitsablauf ausgeführt und die Endergebnisse visualisiert. Der Morphologiefilter mit der Option "Öffnen" und der Filter "Saubere Grenzen" sind vor der Klassifizierung sinnvoll, da sie die Bildmerkmale schärfen. Die Schlussfolgerung lautet, dass die Random-Forest-Klassifizierung die besten Ergebnisse erzielt hat und daher verwendet werden sollte, da sie bei allen NIR-Orthomosaiken hilfreich war; bei den RGB-Bildern war jedoch ein Downsampling erforderlich, um eine angemessene Genauigkeit zu erreichen.

SELBSTSTÄNDIGKEITSERKLÄRUNG

Hiermit versichere ich, dass ich die vorliegende wissenschaftliche Arbeit selbststandig und ohne Hilfe Dritter verfasst habe. Andere als die angegebenen Quellen und Hilfsmittel wurden nicht verwendet. Die den benutzten Quellen wortlich oder inhaltlich entnommenen Abschnitte sind als solche kenntlich gemacht. Diese wissenschaftliche Arbeit hat in gleicher oder aehnlicher Form noch keiner Pruefungsbehoerde vorgelegen und wurde auch nicht veroeoffentlicht.

Autor: Ahmed Abdelwahab
Matrikelnummer: 799717
Universitaet: University of Potsdam
Studiengang: Remote Sensing, geoInformation and Visualization
Titel: Automated extraction of water bodies from NIR and RGB aerial imagery in northern Alaska using supervised and unsupervised machine learning techniques

Ahmed Abdelwahab March 31, 2021-2022

ACKNOWLEDGMENTS

Throughout the writing of this thesis, I have received a lot of support and assistance. I want to thank Alfred Wegener Institution represented by my supervisor, Professor Guido Grosse, for allowing me to work on this topic and facilitate the required resources. I want to thank my second supervisor, Dr. Ingmar Nitze, for his invaluable experience in solving the research questions and methodology. Your insightful feedback and proposed suggestions pushed me forward to achieve this research topic and increase my knowledge to a higher level.

I want to thank and acknowledge my colleagues from my master's program in RSIV at Potsdam University for their extraordinary collaboration. I would like to thank my colleague Shaig Hamzaliev for the support and help in brainstorming and thinking of solutions. Also a special recognition to Sophie Lagarde for the assistance and support with thesis format advises.

In addition, I would like to thank my family for their support and patience through this rough journey. I dedicate all my work to my Son Mohamed Abdelwahab for the inspiration and motivation being away during this journey. I hope this can motivate you in your bright future to achieve more success. I will always be there for you.

Finally, I could not have completed this research without the support of my lovely wife, Yasmin, who played a vital role and support in achieving this.

ACRONYMS

CART - Classification and Regression Tree
DLR - Deutsches Zentrum für Luft- und Raumfahrt
ML - Machine Learning
MACS - Modular Aerial Camera System
NIR - Near Infrared band
RGB - Red-Green-Blue bands
RSIV - Remote Sensing, geoInformation and Visualization
RS - Remote Sensing
RFC - Random Forest Classification
SMS - Segment Mean Shift
SNR - Signal to noise ratio
OOB - Out of bag samples

1 INTRODUCTION

The permafrost was first known in English literature by Muller (1947) to be short term for "Permanently frozen ground soil" [1]. Permafrost condition is to remain below 0 ºC for at least 2 consecutive years. This means that most of the ground soil will be mostly frozen except the material that freeze in lower temperatures than 0 ºC [2] [1]. The active layer of the permafrost is exposed to annual thawing and freezing due to seasonal temperature changes and global warming [1].

The arctic is highly affected by climate change (Arctic amplification)[3]. The Polar amplification means the increase of near-surface air temperature is higher over the Arctic relative to lower latitudes such as than in the planetary average [4][3]. The global temperature rises due to greenhouse gases emissions [5]. Thawing of permafrost regions reveals the long-hidden organic fossils and bodies which emit methane and carbon dioxide gases, contributing to global warming [5]. The biogeochemical cycle has many definitions as it is the pathway by which a chemical substance cycles the biotic and the abiotic compartments of Earth [5]. All permafrost ecosystems starting from wild animals such as polar bears to bacteria, algae and plants consume food and water for their nutrition needs. Therefore any thermokarst abrupt changes affect the hydrological system and harm the lives of living creatures [5][6].

Many human activities contribute to global warming, such as deforestation, fossil fuel burning, fertilizers consisting of nitrogen, etc [7]. In 2017, approximately five million people inhabited around 1162 permafrost communes in the Arctic Circumpolar Permafrost Region [7].

As mentioned above, the warming Arctic can be observed through continuous observation and mapping of the changes in lake hydrology, lake ice characteristics, and permafrost degradation [2]. Therefore, monitoring of lake-rich Arctic regions at high temporal and spatial resolution as well as across very large regions is crucial for understanding their response to climate change and consequently their feedbacks with various environmental conditions [6]. The dynamics of northern high latitude lakes may also serve as a critical climate change indicator or essential climate variable[6].

Remote sensing defined as the process of detecting and monitoring the physical characteristics of an area by measuring its reflected and emitted radiation at a distance. There are different acquisition techniques such as satellite and aerial imagery used to provide information about earth topography [4]. In this thesis, I used aerial imagery collected remotely via special cameras. These images consisted in NIR and RGB bands to measure different physical properties of the permafrost sites.

In order to estimate gas volumes emitted, it is important to be able to map these thawing areas that result in ice-wedge melt ponds. Aerial photographs modelling using orthomosaic allow to identify such areas. Orthomosaic is a method that uses the product of an orthorectified image and mosaicked from image collection, where calibration of geometric distortion and color even-tempered are maintained.

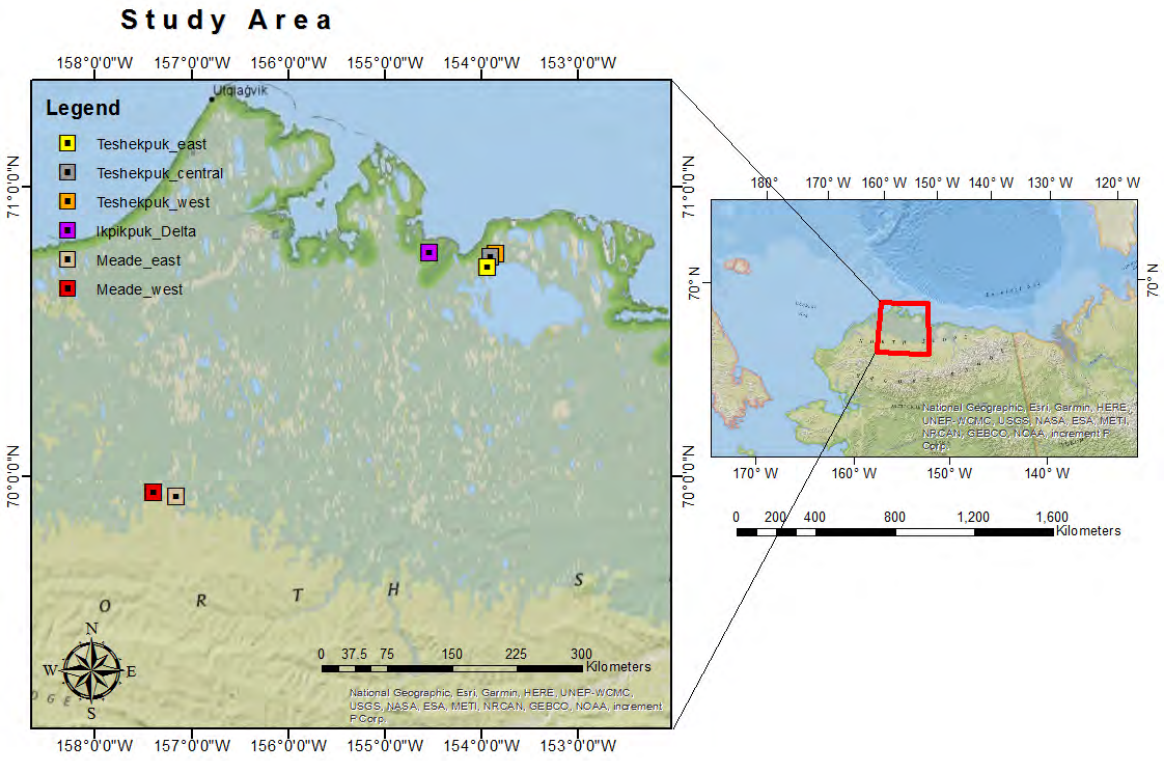

Figure 1.1: The study area location map with the colored pins represent the orthomosaics names in North Alaska, USA

It is a large map with high quality that provides minor details and degradation's. The problem is that it is not always possible to discriminate water bodies in the orthomosaics images as they are sometimes blended in the environment. Thus, in this thesis, I first tested machine learning methods (RFC, SMS and KM) on a small sample of images to identify automatically the pixel type and thus detect water bodies. The chosen three different sites in figure(1.1), have different types of ponds and water polygons (It will be explained in Study area section 2.1).

After validating the algorithm on this image sample, the algorithm are applied on the whole Orthomosaic image in order to detect the water bodies. The figure 1.1 shows the study area of my topic, located in northern Alaska, using areal photogrammetry data captured in 2019 by Thaw Trend Air 2019 flight campaign.

My study aims to answer three main scientific questions; how accurate water bodies can be extracted using machine learning techniques? Which ML methods are adequate for water bodies mapping either supervised or unsupervised techniques? Is there any difference between NIR-based and RGB-based classification for water bodies mapping?. The following chapters will provide results and a conclusion to the previous questions.

1.1 DATA COLLECTION

The airborne photogrammetric images were acquired in northern Alaska during July 2019. As mentioned in chapter 2, July till September is the summertime in Alaska; thus, it is good to observe the water bodies' degradation through warm periods. The following table (1.1) represents the data used for this study:

Area	RGB Images	NIR Images	Spatial resolution	Altitude	Latitude (DD)	Longitude (DD)
Ikpikpuk Delta	6	6	4-7 cm	460-480 m	70.80	-154.46
Teshekpuk Central	6	3	6.4-10.6 cm	740-770 m	70.76	-153.87
Teshekpuk East	6	3	6.2-10.3 cm	725-750 m	70.81	-153.54
Teshekpuk West	6	6	6.3-10.8 cm	758-760 m	70.76	-153.87
Meade East	4	5	8-13.8 cm	1026-1028 m	69.95	-157.37
Meade West	4	4	7.9-13.5 cm	1004-1013 m	69.96	-157.13

Table 1.1: Input test aerial images information

As per table (1.1), the spatial resolution of the aerial images increases with higher altitudes. Therefore, Meade data has higher spatial resolution than Ikpikpuk, thus more details. Processing steps went through three main phases: pre-processing, filtering and images classification.

1.2 THESIS OUTLINE

This thesis focuses in two steps. The first step is testing supervised and unsupervised machine learning classification algorithms to extract water bodies from aerial imagery, and choose the more adapted algorithm. The second step consist in applying this algorithm to the orthomosaic in order to extract water bodies from aerial imagery. The general layout of this process is illustrated in figure 1.2. In Chapter 1, the introduction to data-set type. Chapter 2, the study sites are introduced with aerial imagery examples.

The method is given in chapter 3, first, the automated ML techniques used to perform image classification are described 3.1. Second, image pre-processing is given in 3.2. Third, the classification process using algorithms is given in 3.3. Then, the pre-processing and post-processing of the images to improve image quality using filters are described in 3.4. Then, the assessment of the classification algorithms given in 3.3 is done in 3.5. Finally the assessed algorithms are used on the Orthomosaic in 3.6.

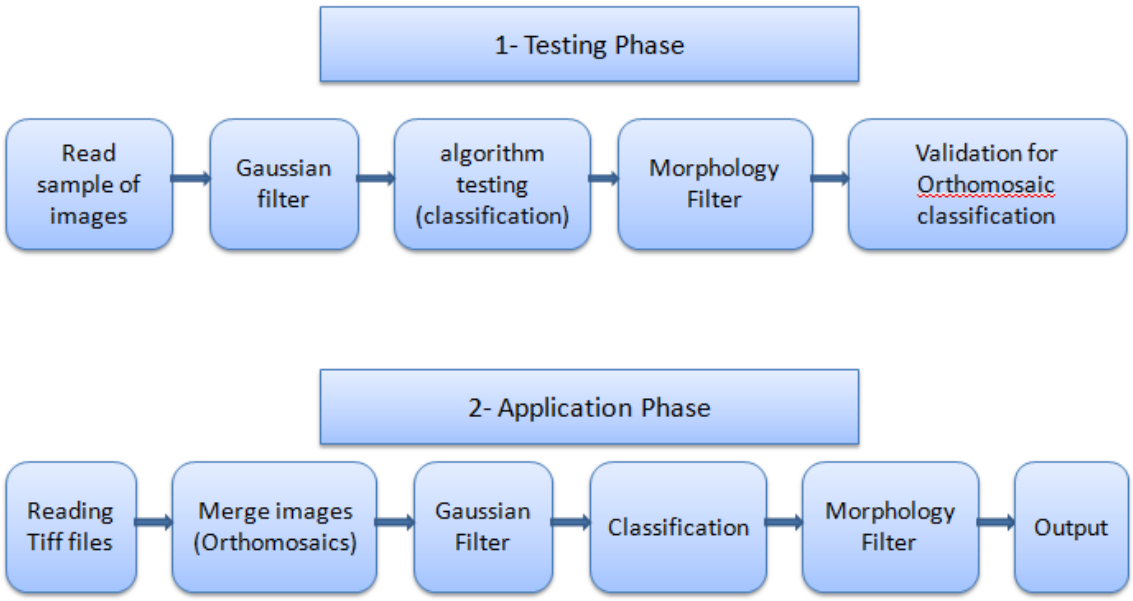

Figure 1.2: Machine learning classification workflow

Chapter 4 presents the results of the proposed workflow. In Chapter 5, results are discussed. Chapter 6 is devoted to summarizing and concluding the thesis with a possible outlook.

2

STUDY AREA

2.1 STUDY AREA

Our study area location is the north-eastern side of the Arctic Coastal Plain of the U.S. state of Alaska, close to the border of Canada. The Alaska North Slope site has a continental arctic climate with a mean annual precipitation of 115 mm at Barrow and a mean annual air temperature of 11.2° C (NOAA, 1981–2010). The mean annual temperature explains the reason The land cover is covered by low tundra vegetation as well as surface water bodies.

Figure 2.1: Alaska Köppen Climate zones (Perkins, R., 2010)

The climate zone of North Alaska where all our chosen sites considered as Arctic zone (2.1). It was first published by German-Russian climatologist Wladimir Köppen (1846–1940) in 1884. This type of climate has every month of the year with an average temperature below 10 °C. It has two main sub-zones: Tundra climate and Ice cap climate and our sites belong to Tundra climate where the average temperature for the warmest month is between 0 °C and 10 °C.

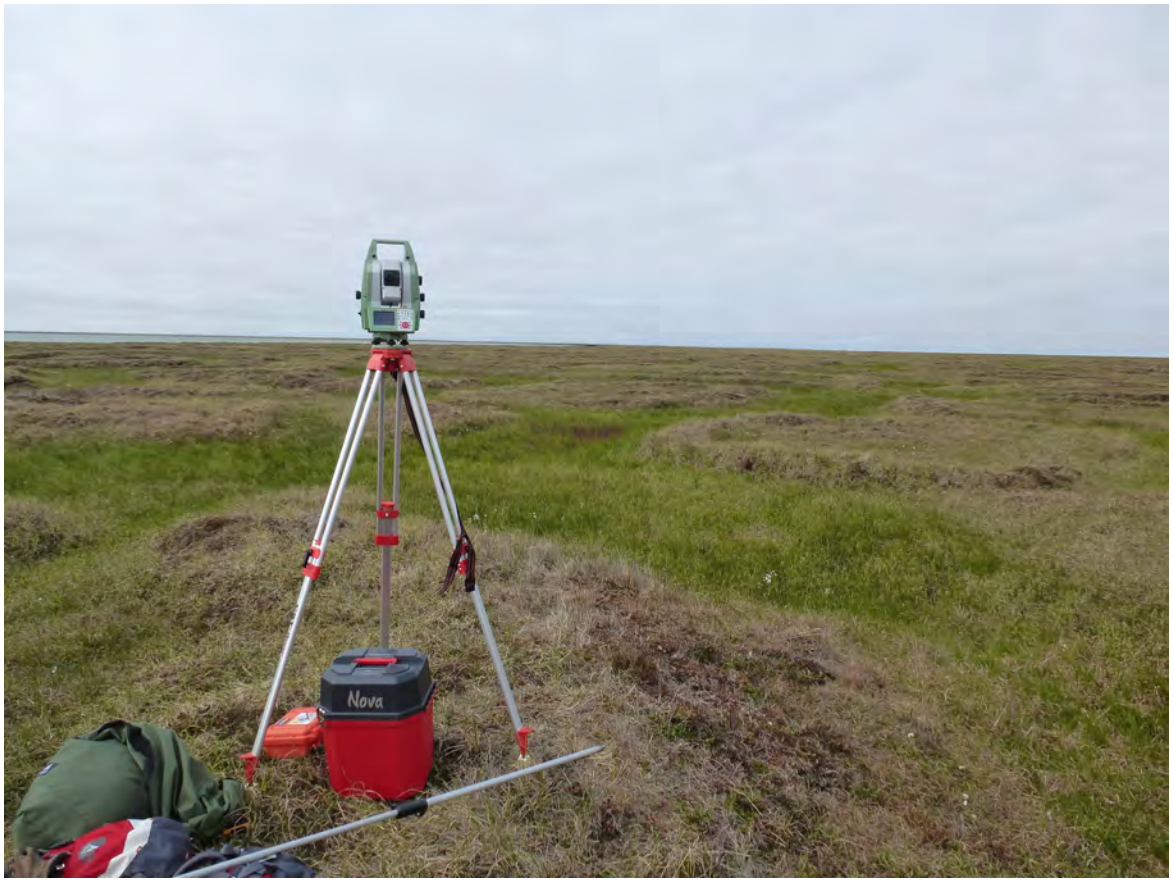

Figure 2.2: Photo for Teschekpuk East for Tundra vegetation (taken by Thaw Trend Air 2019 flight campaign)

It is also near the shoreline of the Beaufort Sea. The northern coast witnesses an arctic climate (2.1), allowing plant growth in late June, July, and August. This tundra vegetation appears clearly in the captured field photos as per figure (2.2).

To test the algorithms used to identify the pixels type on the Orthomosaic image, a sample of images from each area described below was taken. For each area, the number of samples for each RGB and NIR images is given, as well as the labels chosen for the classification.

Polygonal ice-wedge networks are standard throughout areas of continuous permafrost [8]. I aim to extract the near-surface ice wedges and polygons since I have surface aerial photogrammetry. I have 3 different sites (Ikpikpuk, Teshekpuk and Meade) each contain 3 different characteristics to test the efficiency of the workflows. The most outstanding characteristic of the Teshekpuk Lake site is the large, directionally-oriented thaw lakes and second- or later-generation wetlands [9]. Wetlands include around 30% of the site and vary in size from flooded tundra depressions to thaw lakes up to 14.5 km in length [10]. The Lakes west of the Ikpikpuk river are generally more shallow than those to the east and few of the deep basin lakes found in the eastern area are found west of the Ikpikpuk river. The third site is Meade which contains relatively small lakes as it is far from water sources and shoreline.

2.1.1 *Teschekpuk Site*

Teschekpuk site has three different locations as shown in figure (2.3). The area contains the Teshekpuk Lake, which is the largest lake in Arctic Alaska and the largest thermokarst lake in the world [10].

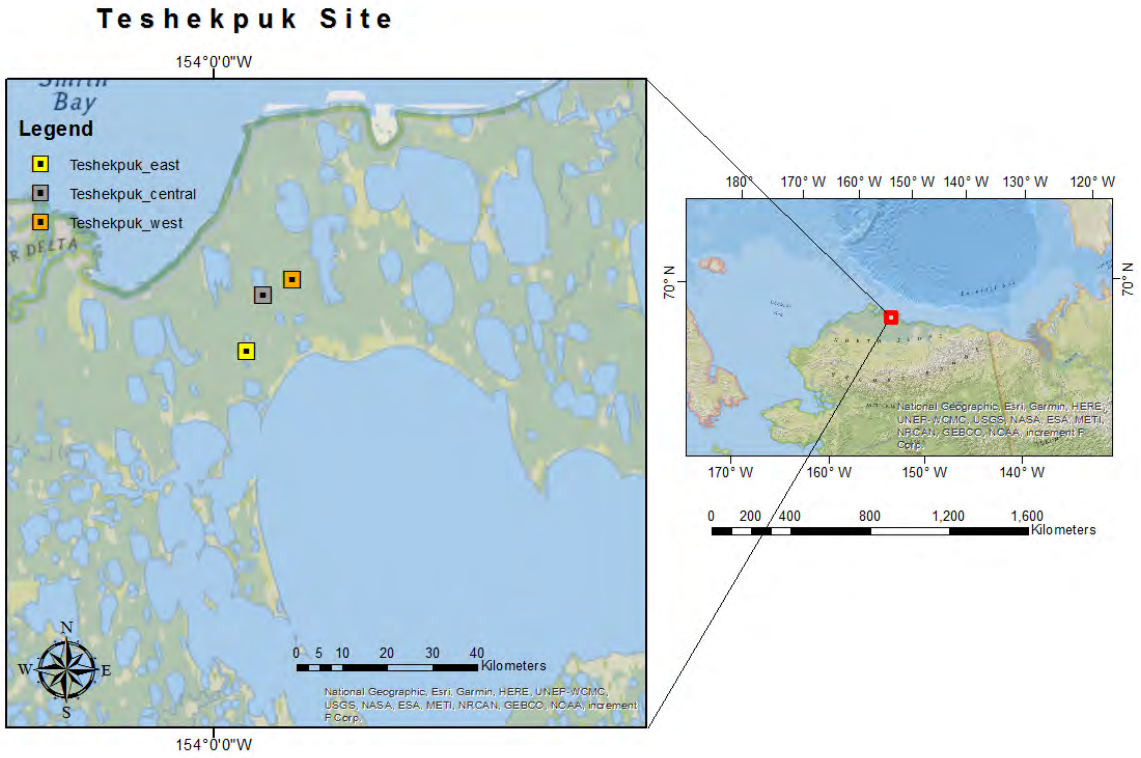

Figure 2.3: Teshekpuk maps respectively from right to left (West - Central - East)

The common characteristics between the east, central and west is the relative wide spread water polygons in comparison to the Meade and Ikpikpuk delta sites. The soil is influenced most likely by sediment entrained from the sea floor deposits and fine-grained ice-rich sediments lie along the northern shore of Teshekpuk Lake and organic matter in the area are generally HisticPergelic Cryaquepts and Pergelic Cryofibrists, indicating cold (usually less than 0°C) wet soils with surface horizons with high content in inorganic matter [11]. The closeness to the shoreline and all above-mentioned conditions means the Ice wedge polygons are mainly high centered and wide lowlands and most of the Polygons are dry as per figure(2.4).

Figure 2.4: Teshekpuk airborne photo showing the landscape (taken by Thaw Trend Air 2019 flight campaign)

In figure (2.4) there are wide lakes spread along the Teshekpuk site. A prominent characteristic of the Teshekpuk Lake area is the large, directionally-oriented thaw lakes and second- or later-generation wetlands [9].

(a) RGB aerial image

(b) NIR aerial image

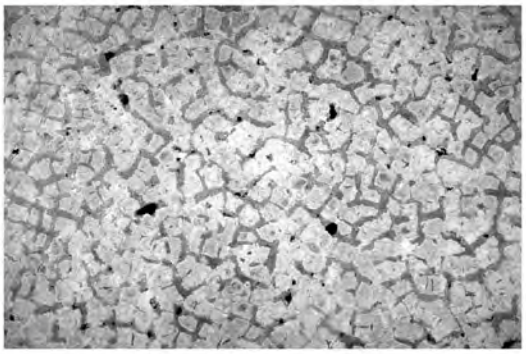

(c) Teshekpuk photogrammetry coverage

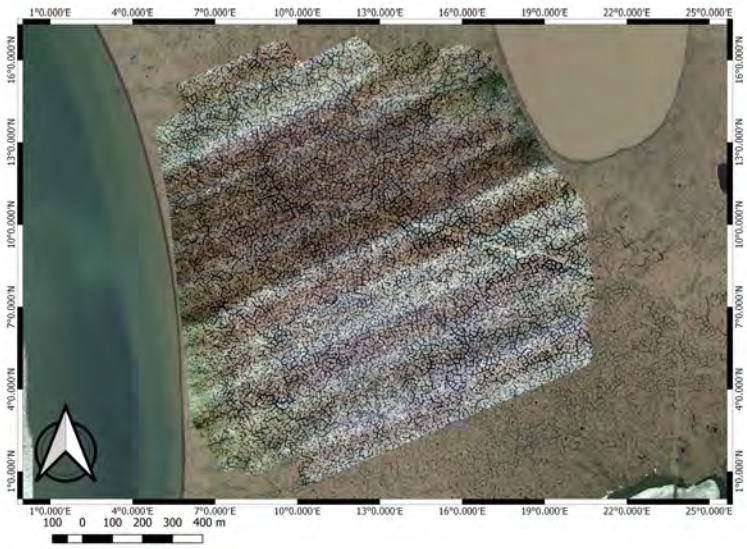

Figure 2.5: (a) RGB sample image, (b) NIR sample image, (c) ESRI satellite image representing the aerial imagery coverage for Teshekpuk site.

The Teshekpuk site contains two types of water surfaces: a relatively deep and clear water class and a shallow water class with some water algae and vegetation (2.5). The Teshekpuk classification consists of four classes: Pasture (dry sedge-Meadow), Water, Shallow Water, and Wet Vegetation (wet sedge-Meadow). However, in the Teshekpuk East, we have only three classes: Pasture (dry sedge-Meadow), Water, and Wet Vegetation (wet sedge-Meadow). The class names used are simplified such as Pasture which is dry sedge-Meadow and wet vegetation is wet sedge-Meadow. Lake formation and drainage are widespread in permafrost regions. Drained lake basins are usually a frequent feature in lowland permafrost regions in the Arctic.

2.1.2 *Ikpikpuk Delta*

This site located in the Arctic Coastal Plain in the middle of Ikpikpuk delta. It is near the Ikpikpuk river with a large central lake on the eastern side and the Ikpikpuk river from the western side. Ikpikpuk location as shown in figure (2.6), presents more large lakes compared to the other sites. However, the vegetation reflection represents some differences and leads to complications, especially for the RGB images.

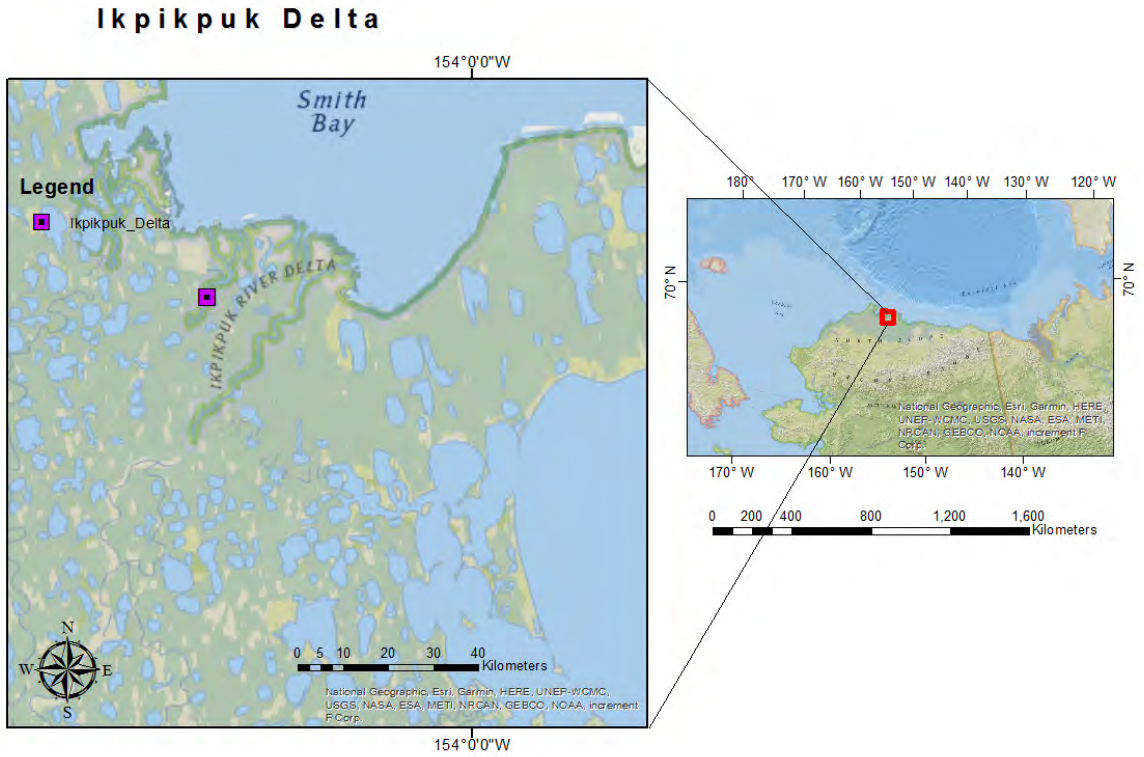

Figure 2.6: Ikpikpuk delta aerial imagery location map

Ikpikpuk delta is characterized by typical fluvial and deltaic processes such as tides, periodic flooding, sediment deposition, channel migration, and shoreline erosion (2.7) [12]. This means the lakes build up mainly from a peak discharge during the time of river ice break-up, and a declining discharge until freeze-up. There is no discharge in the winter compared to low-latitude river deltas [12].

Figure 2.7: Ikpikpuk delta airborne photo showing the landscape (taken by Thaw Trend Air 2019 flight campaign).

The landscape area has a geologic history, permafrost-ice material, and subsurface thermal regime. The Ikpikpuk River is a meandering stream on the Alaska North Slope with a low height gradient. This explains the presence of low centered ice wedge polygons and wide lakes.

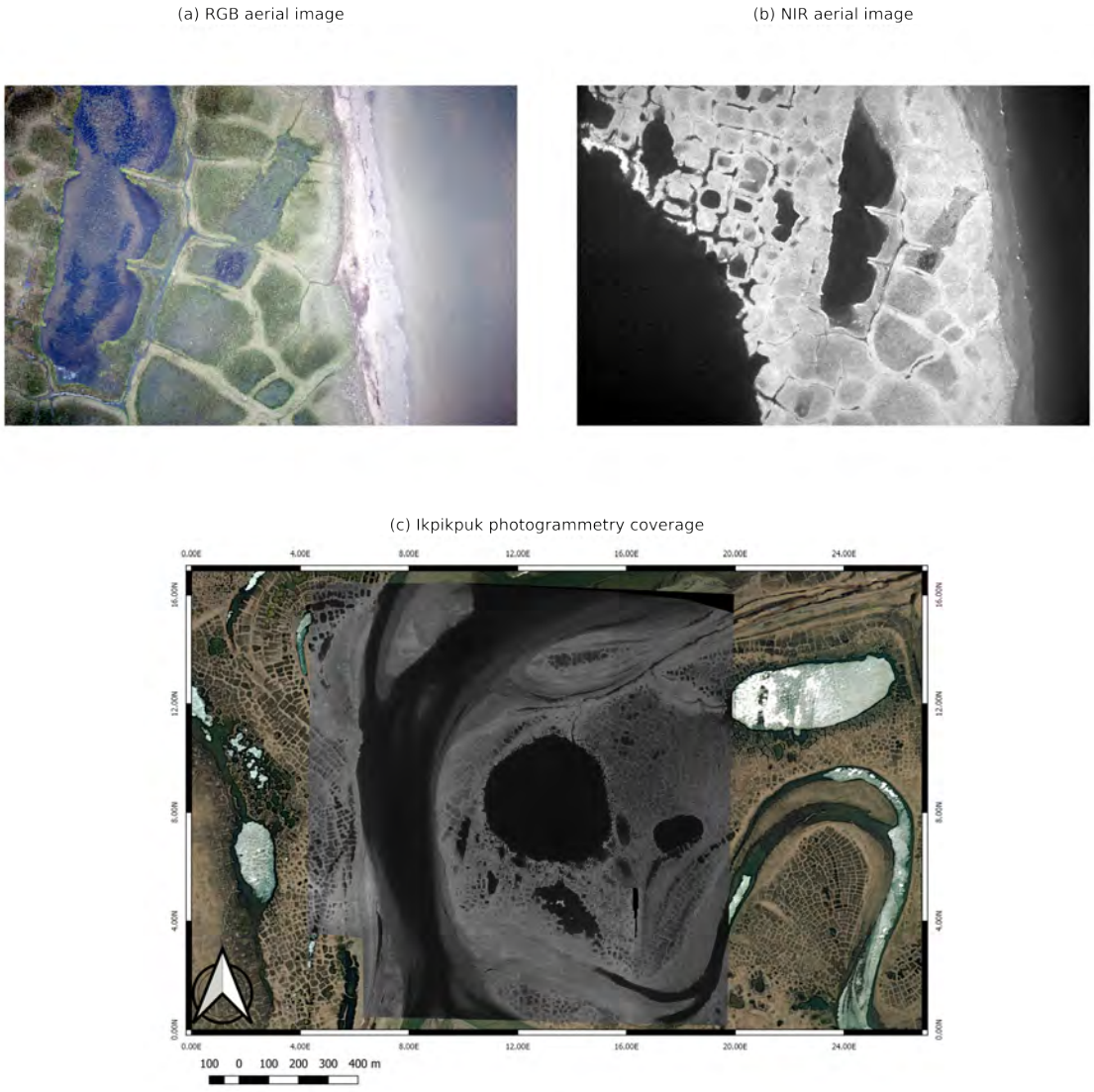

Figure 2.8: (a) RGB sample image, (b) NIR sample image, (c) ESRI satellite image representing the aerial imagery coverage for Ikpikpuk.

Thermokarst land-forms cover the entire region, and the distribution of thermokarst land-forms and overall landscape complexity is significant with surface topography and geology (2.8). The Ikpikpuk Classification consists of four classes: Pasture (dry sedge-Meadow), Water, Shallow Water, and Wet Vegetation (wet sedge-Meadow). Drained lake basins are a regular feature in lowland permafrost regions in the Arctic. Therefore it was intricate to map the water surfaces, especially in RGB images, as they contain more details and similarities between shallow water and drained lakes pixels.

2.1.3 *Meade Site*

The Meade area is inland far from south of the Beaufort Sea, and its weather and topology characteristics of both the shoreline and the domestic Arctic cause the water bodies to be relatively small sizes. Although the terrain is mostly flat and has no trees, it is called "Upland" as it has more terrain than the other two sites and is distinguished by tundra vegetation and small lakes, as shown in figure (2.9).

Figure 2.9: Meade airborne photo showing the landscape (taken by Thaw Trend Air 2019 flight campaign)

Meade site, as shown in figure (2.10), has less lakes compare to the other sites. However, the vegetation covers most of the terrain and present less differences compared to the water surface and lead to complications in NIR as there was a shadowing effect. The common characteristics between the east and west is the presence of relatively small lakes of water polygons in comparison to the Teshekpuk and Ikpikpuk areas where they are bigger.

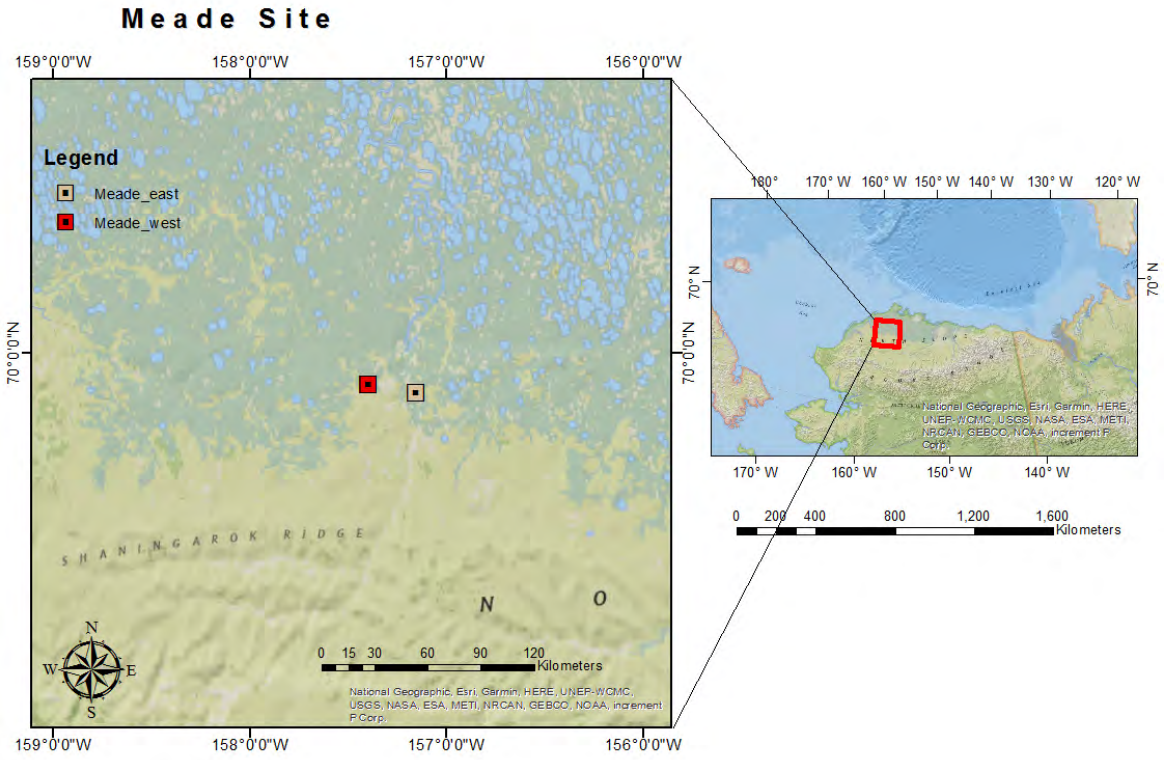

Figure 2.10: Meade maps respectively from right to left (West - East)

The diminution of lake basins is a usually frequent feature in this permafrost region. Therefore, it is very challenging to map the water surfaces (2.11). The small water bodies are caused by the lack of water sources such as rivers and seas.

(a) RGB aerial image

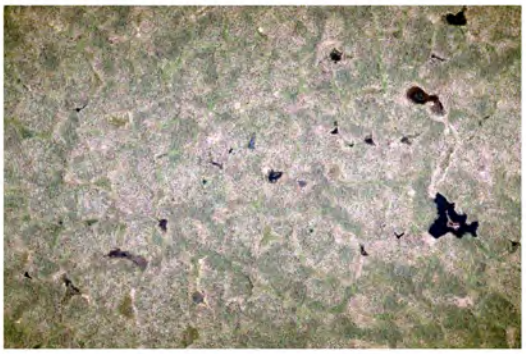

(b) NIR aerial image

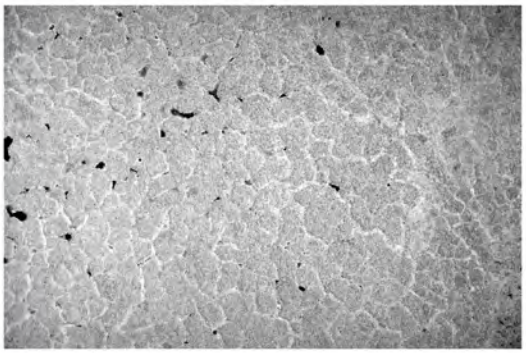

(c) Meade photogrammetry coverage

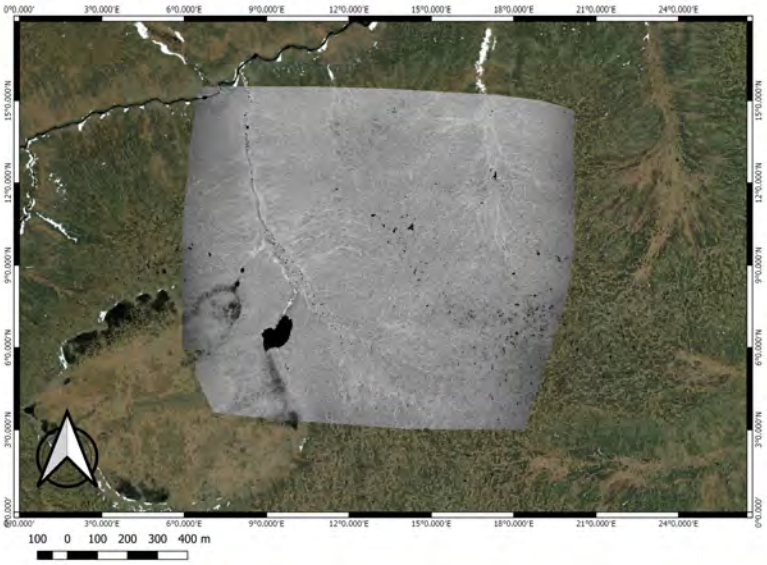

Figure 2.11: (a) RGB sample image, (b) NIR sample image, (c) ESRI satellite image represent the aerial imagery coverage for Meade site.

Small-scale patterns of distinct plant communities related to ice-wedge polygonization are characteristic of the region. There are small dissiminated water bodies and small high centered polygons due to the lack of water sources in this site.

3

METHODS

3.1 REMOTE SENSING ML CLASSIFICATION REVIEW

Machine learning classification is a frequently applied technique in remote sensing (RS), spatial classes defined are critical for obtaining accurate results and achieving maximum precision. There are three ML classification methods: supervised, unsupervised, and hybrid [13]. The unsupervised ones require no training pixels and more parameterization. The supervised classification technique relies on training pixels to define all classes [14], [15]. The hybrid classification technique is a mixture of unsupervised and supervised classification techniques [16].

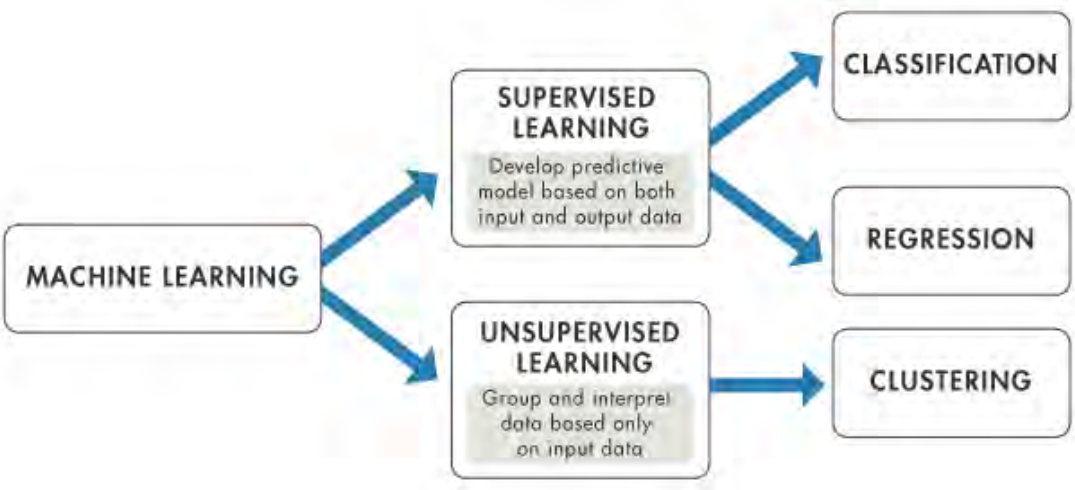

Figure 3.1: Machine learning classification workflow

As per figure (3.1), the unsupervised classification groups the input data based on internal interpretations by the algorithm. The supervised classification uses input training pixels and input data in order to predict the output data. The supervised learning technique assemble a defined input pixels data and train a model in order to generate a reasonable predicted output data. There are two types of supervised learning techniques which are classification and regression model methods:

- Classification techniques are based on feature responses. For instance, our data is aerial imagery representing the light band intensity reflected on the Earth surface.
- Regression techniques are based on temporal responses, such as variations or fluctuations in precipitation or temperature. Regression techniques are commonly used in forecasting applications.

In this thesis, I tested only the supervised and unsupervised classifications.

3.1.1 *Supervised classification*

In this thesis, ML random forest classification (RFC) and segment mean shift (SMS) are the supervised algorithms used. The motivation behind choosing RFC is that it seeks to minimize the heterogeneity of the image pixels, which can serve the purpose of water ponds extraction from the surrounding data pixels. Random forest algorithm is a group of tree predictors such that each tree depends on the values of a random vector sampled independently and with the same distribution for all trees in the forest [17]. The random forest classifier requires two main parameters [18]:

(1) number of classification trees.
(2) The input variables number considered to each node split.

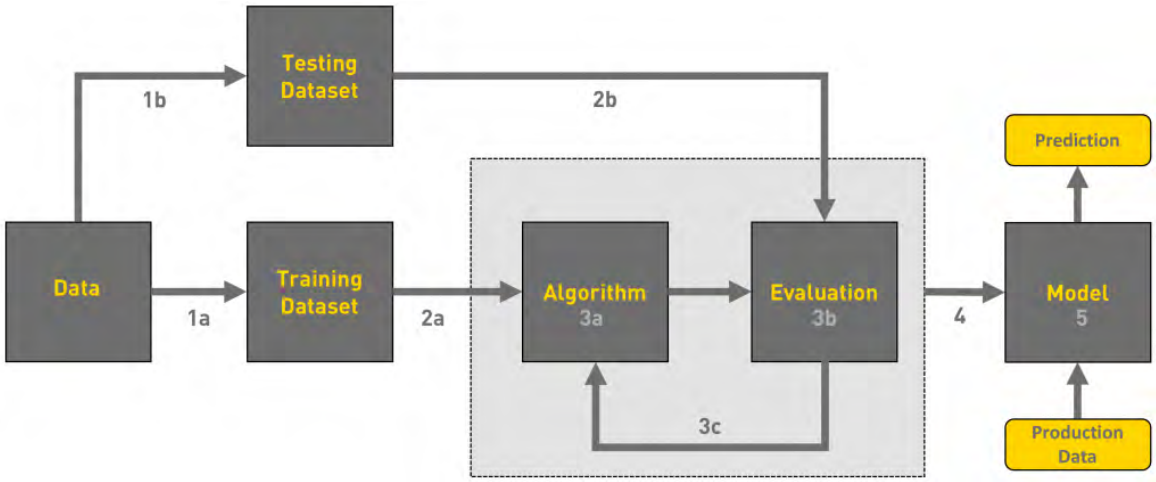

Figure 3.2: Machine learning supervised classification workflow

As per figure 3.2, the input to the classification are the data and training dataset. The workflow shows that we use the training data to initiate the algorithm running. The algorithm is then tested with the True data (Training dataset). After an evaluation (3b) of the testing data, once the algorithm is approved, it is used to model the input data set and predict the labels.

However, the SMS provide noise filtering to tackle the complexity of some images due to topology, vegetation and shadowing effect. The segment mean shift is a centroid-based algorithm used in supervised learning cases. It is one of the practical algorithms used in image processing and computer vision. This technique works by shifting data points toward centroids to be the mean of other pixels in the region. One of the challenges faced, especially for the Meade site, is its thorny shrubs and vegetation with small water bodies.

3.1.2 *Unsupervised classification*

The unsupervised classification algorithm detects the patterns and internal structures in the image. It aims to use these patterns and similarities of the image pixels without using any labels or training samples [19]. The K-mean is a method of vector quantization, originally from signal processing, that aims to partition n observations into k clusters, requiring less computation.

This technique is useful for large number of pixels as it would be memory costly to use input training data or uncertainty about the number of labels in our clustering; because, this can be forecasting of the data patterns and groups. Unsupervised machine learning classification has two main categories:

- Parametric unsupervised learning: this category assumes that the data has a normal distribution. In other words, the sample data generated from a population follows probability distributions of unique sets of parameters. Therefore, all group pixels have the same mean and standard deviation parameters.
- Non-parametric unsupervised learning: the data is clustered in groups in this version, each in terms of categories and classes present in the input image. The nonparametric models require no assumptions by the user about the population distribution, which is the reason behind the name of the "distribution-free method".

3.2 IMAGE PRE-PROCESSING

3.2.1 *Devignetting*

The vignetting phenomena are natural effects that occur due to the camera lens [20].Input aerial imagery has vignetting/edge effect which needs to be corrected. Generally, it results from lenses with wide apertures. The camera sensor is flat, therefore most of the light beams reflected through the lens hit its centre while the light from the far pixels usually hits the boarders area of the flat sensors with an angle. Hence, the edges of the images are darker [20]. Even if companies make efforts to manufacture lens with minimum vignetting effect, it still exists to a low level in all lenses [20].

As shown in figure 3.3, there are illumination variations from center toward the edges for all presented bands. It is so distinctive in the corners and edges of the image compared to the centre of the image that faces more the centre of the camera lens.

This variance leads to inaccurate classification in the corners, misleading for Orthomosaics segmentation and merging. To correct the vignetting, we used the DLR Macs-box tools (MACS). MACS tools have effective filters that process each band separately and balance the brightness according to neighbouring pixels. Figure 3.3 represents the shadowing effect in RGB bands which leads to inaccurate classification results at the edges.

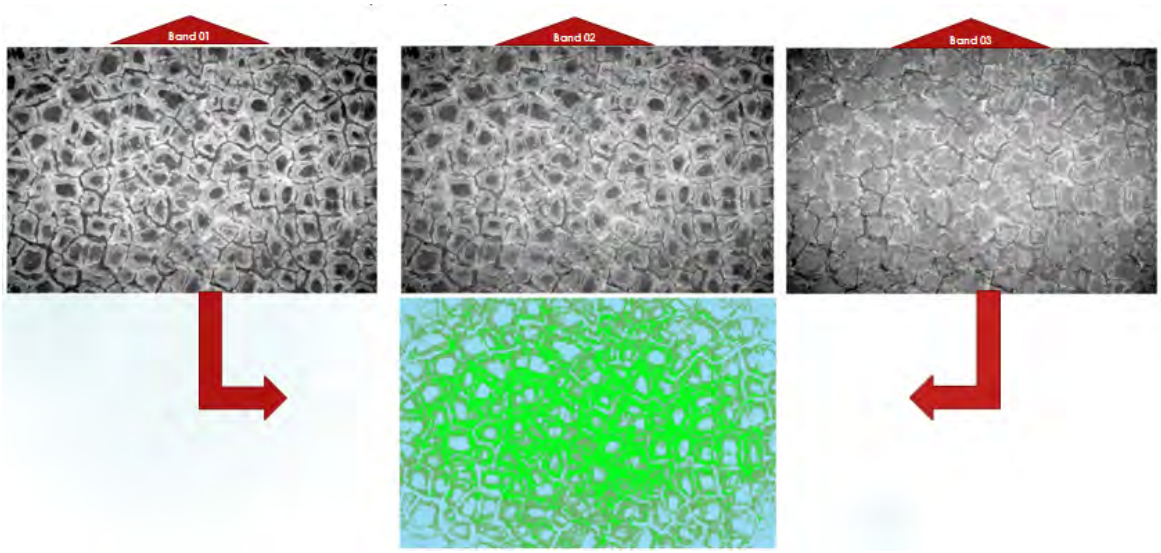

Figure 3.3: Teshekpuk RGB Image bands before and after classification showing the issue with classification (green represent the vegetation and blue represent the water)

The edges of all bands were darker and caused a misleading classified pixels as per figure (3.3). This is the reason to apply Devignetting filter is needed to retain the pixels from the edges.

The equation 3.1 represents the vignetting correction to each pixel, where "offset" is the normalized distance from the raster image centre:

$$pix_{corrected}(i,j) = (pix(i,j) - offset(i,j)) * factor(i,j) \tag{3.1}$$

Parameter name	Definition	Parameter used
offset	This value will be subtracted from every pixel in the image.	0
factor	Every pixel in the image will be multiplied with this value.	1
Offset Image	If provided, the values in the linked file will be used as offsets on a per pixel basis.	<none>
Factor Image	If provided, the values in the linked file will be used as factors on a per pixel basis.	<none>

Table 3.1: Devignetting applied parameters

In figure 3.4, the filter balanced the reflected colours spatially from the centre of the image towards the corners and edges.

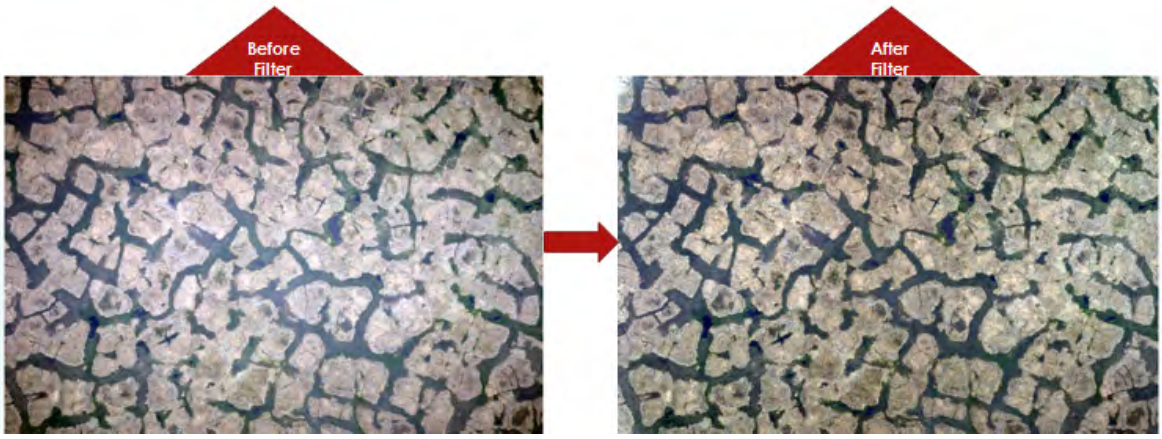

Figure 3.4: Teshekpuk RGB Image before and after Devignetting

The DSNU filter applied to all images with the selected parameters as per Table 3.1 in order to balance the shadow effect in the image corners.

3.3 IMAGE CLASSIFICATION

The success of the remote sensing technique is valuable among all other mapping fields in terms of image classification due to vast reasons, especially the choice of optimum classification algorithm [21]. The images provided consist of two types of data, multi-band (RGB) and single-band (NIR). I tested three different machine learning techniques to find a good workflow for each data type. The machine learning workflow shown in figure 3.5

has two distinct inputs to the algorithm: training labels (user-defined) and training data. It uses the labeling of image pixels, saves them, debugs models, and continually improves model accuracy.

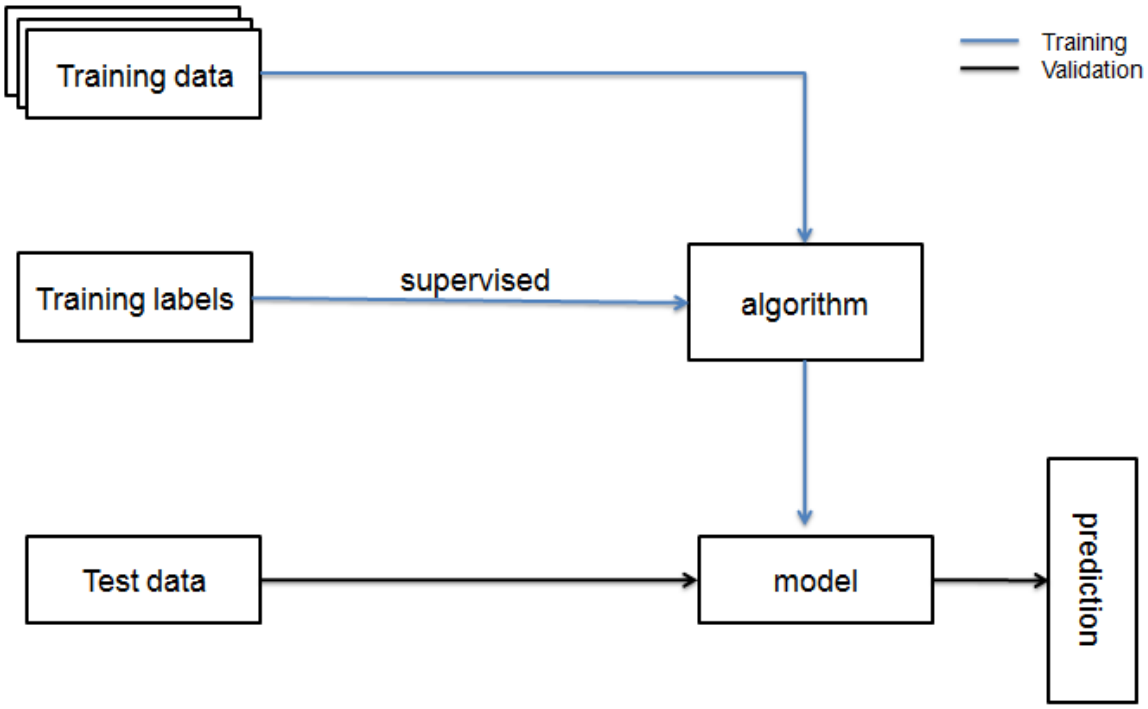

Figure 3.5: Supervised machine learning workflow

The idea encouraged me to use a generalized workflow, which gives the best average accuracy among all other algorithms and adequate for both image bands NIR and RGB.

3.3.1 *Unsupervised K-Means classification*

Extraction of specific features is one of the essential stages of the identification system, and the main aim is to classify the dominant attributes of the raster image [19]. The more distinctive features lead to successful classification and recognition by the K-Means algorithm and vice versa [19].

The color segmentation technique defines each overall color (NIR) or combination (RGB) marker and labels them with values [22]. After this, the similarity of each pixel point and the surrounding neighbouring pixels region is evaluated [22]. The K-means method processes every feature with a pixel location spatially and finds groups so that features among every cluster are as close as possible to each other and as far as possible from elements in different collections [22].

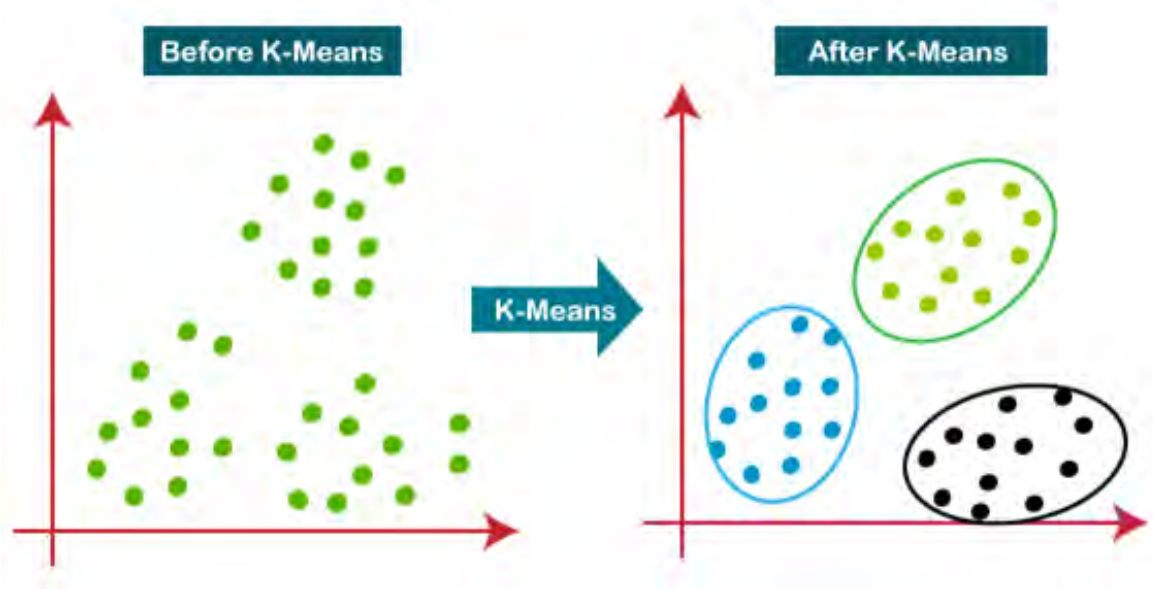

Figure 3.6: Plot representing ML K-means Clustering algorithm [23]

Figure 3.6 shows that the K-means algorithm typically detects a pre-defined number of clusters among all unlabelled input images. It performs that via simple criteria to what will be the flawless clustering for all pixels [23]. The main two concepts are:

- The "cluster center" is the arithmetic mean of all the pixels being the possession of the cluster.
- Every pixel is closer to its cluster center than other cluster centers.

The precession of each class is to have well-defined centroids or centers so that the clusters will be well separated [23], following the equation:

$$c_j = \frac{1}{n_j} \sum_{d_i \epsilon c_j}^{n} d_i \tag{3.2}$$

As per equation 3.2 where d_i represents the object number $_i$, c_j represents the cluster centroid of cluster $_j$, and n_j is the total number of objects in cluster $_j$ [23]. The advantage of K-means unsupervised classification is that the parameters are used only to define how many classes you will use (number of clusters). I chose four sets for the RGB images, and for NIR images, I decided on three groups as they present fewer details than RGB.

3.3.2 *Supervised segment mean shift classification*

The segment means shift algorithm is widely used in clustering, segmentation, and filtering [24] [25]. The mean shift algorithm picks the mode value of the probability density

function based on kernel density estimate [26]. Therefore, I choose this ML technique as it is useful for noisy data and can optimise the Meade site as per previous statement.

$$\widehat{\nabla} f(x) \equiv \nabla \widehat{f}(x) = \frac{1}{nh^d} \sum_{i=1}^{n} \nabla K \left(\frac{x - x_i}{h} \right) \tag{3.3}$$

In this equation 3.3, h represents the window kernel of K. n stands for the number of d-dimensional vectors x_1 to x_i. In the segmentation case, each feature vector contains color/intensity information and the spatial position of the pixel [27]. The mean shift algorithm is a mode pursuing technique in a density distribution with no previous computation for the distribution [27].

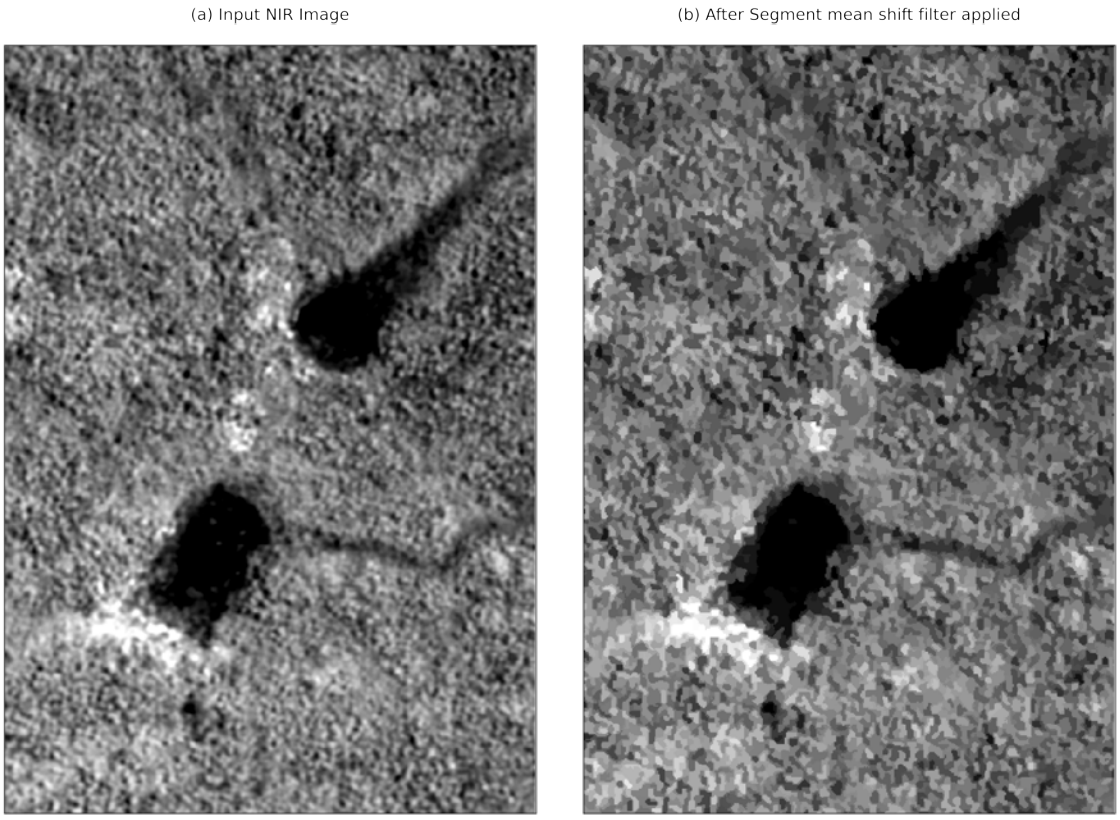

Figure 3.7: (a) Meade East aerial image before segment mean shift (b) Meade East aerial image after segment mean shift algorithm

The segment mean shift technique is a powerful clustering technique, based on detecting modes in a probability density function iteratively [27]. In the Meade area, there are complex and rough topography, causing a spatial reflectance variance leading to shadow and dark pixels. Those dark pixels are small enough to cause issues to the classification algorithm since they are in each training sample 3.7. The effect of the filter is not entirely obvious in figure 3.7; however, the final resulting classified images are cleaner and better in quality. The segment mean shift tool in Arc-gis helped reduce the shadowing effect by using the superpixel clustering and 20 hyper-spectral bands (Parameter used to define the number of spectral range of SMS new pixels) to distinguish only the relatively dark pixels

that belong to water or lake surfaces. We believe that only the water surface, which is > 10 times the pixel size, will remain the same.

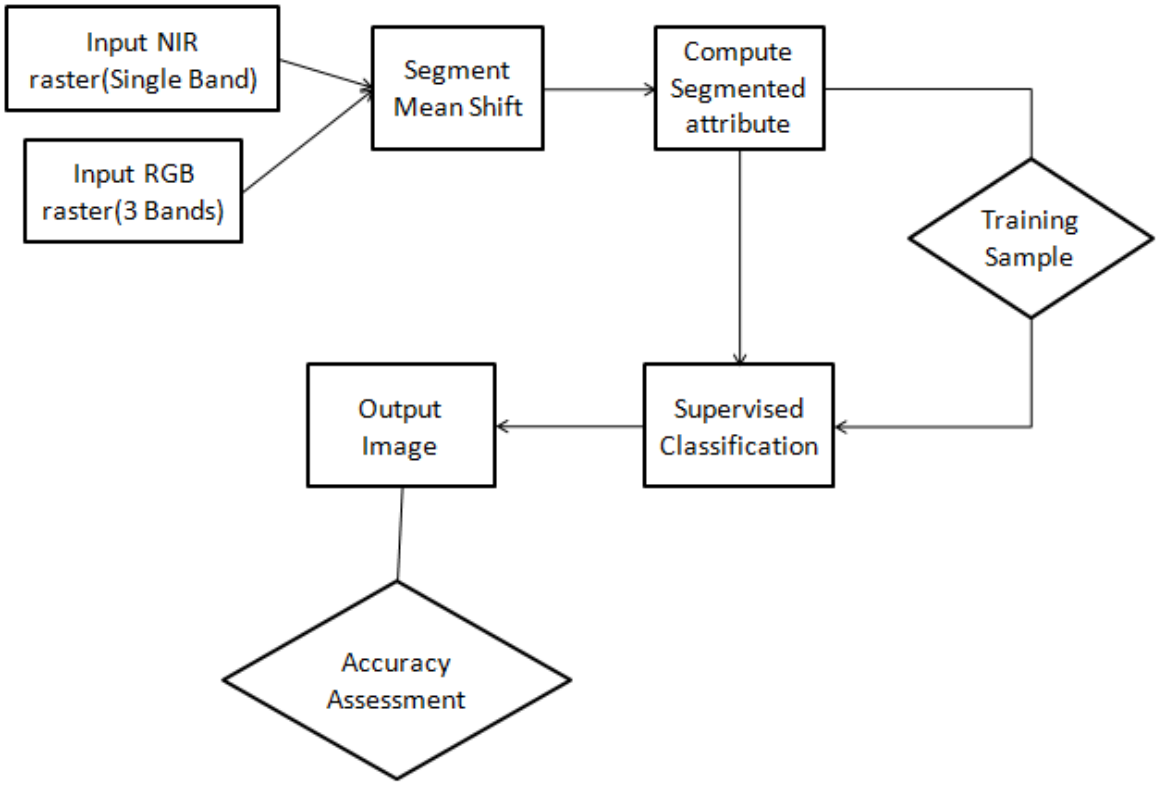

Figure 3.8: Segment mean shift supervised classification work flow

The workflow displayed in figure 3.8 presents the steps pre-classification. First, selected bands from the image are read, either 3 in RGB or 1 for NIR. The computation of segmented spectral requires the main parameter: the labels or attributes you choose to be used for analysis. The next step is grouping the segmented pixels based on the similarity in characteristics.

Here, we choose an attribute, the spectral range, as the main parameter for the classification, and the valid values range from 1.0 to 20. The higher spectral range leads to small details and features clustered together. The smaller values create a spatially smoother classified image. In provided data, I choose value 10, which is an intermediate result to avoid shadow pixels. Finally, the accuracy assessment was done by using random points selection to validate the results.

3.3.3 *Supervised random forest classification*

The supervised classification algorithms provide adequate output only when the input image is a single band dataset. However unsupervised algorithms such as Maximum likelihood (MLC) multiband images, for instance RGB-satellite images, have limitations as the algorithm's classifiers assume a normal data distribution [13].

The random forest classification technique is a clustering classifier that uses a group of the Classification and Regression Tree (CART) to perform prediction [17]. These decision trees are made using manual training samples via the substitution approach (bagging), which means the same data will be selected multiple times, and others may not be chosen [17].

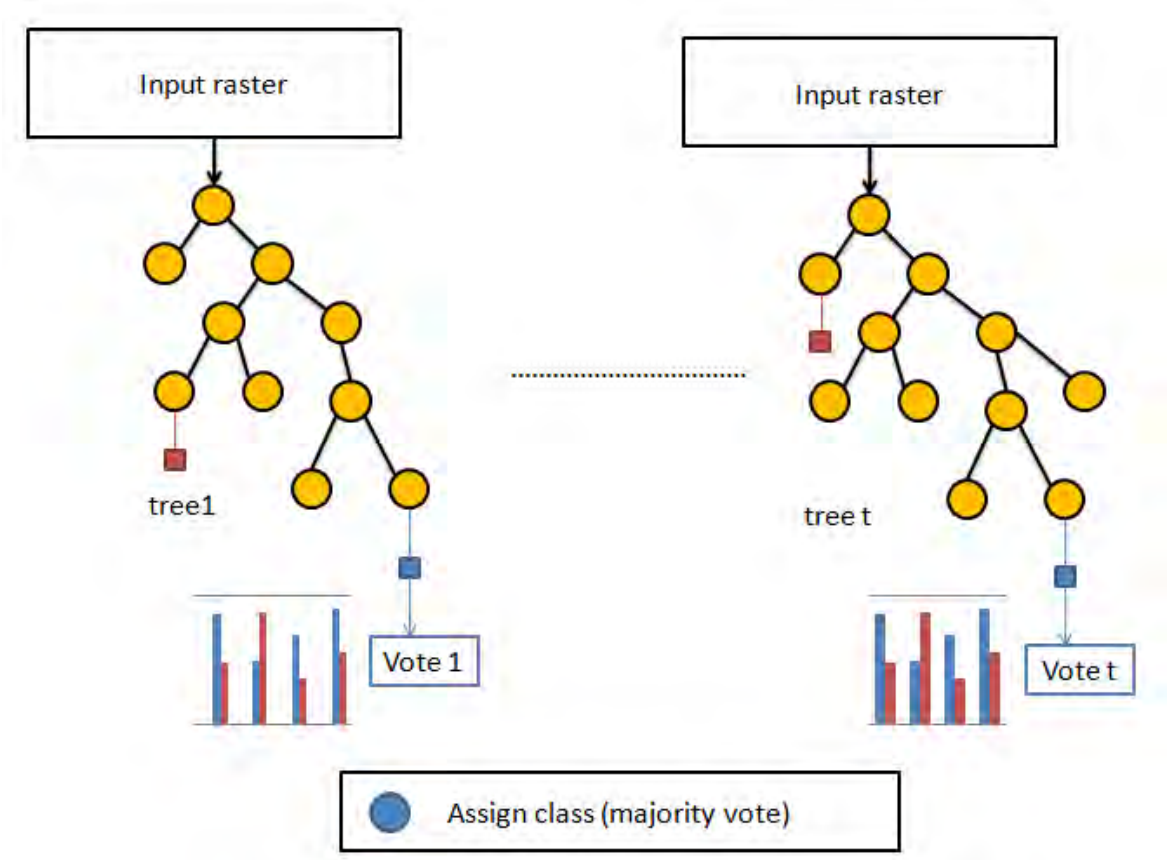

Figure 3.9: Random forest classification decision trees and bagging trees (based on Belgiu, M., 2016).

As shown in figure 3.9, two-third of the samples are selected by the bagging trees, but one-third is not chosen and is labelled as OOB (out-of-bag samples). This OOB error will be used during the cross-validation to validate the accuracy of random forest classes [17].

The decision tree is independent and split based on a user definition of how many features (M) were picked at random. Once the number of tree grows, the RF establishes D-trees with low bias and high variance [17]. The last RF classification tree will be averaging (using the arithmetic mean) the class probability estimated for all output trees. The output trees will be validated with the input image using a voting process. The class with the highest votes will be the approved class [28].

In practice, the RGB and NIR images have similar workflow and parameters. This technique depends on the provided training sample as it is supervised classification. The validation parameters use 25 % of the original data labels and predict 75 % using the random

forest classifier model. The accuracy assessment was performed based on the training data validation.

3.4 IMAGE FILTERING

There are two primary filters used through this stage: Morphology filter and Gaussian filter. The Morphology filter was developed in the early 1960s by Matheron (1975) and Serra (1982). The filter aims to shrink minor outliers and features using the median filter to preserve and merge the significant features and filter out the minor features [29]. The Gaussian filter is a two-dimensional digital filter relying on sigma (σ), the variance or standard deviation of the dominant pixel values, and applies a range of sigma to suppress noise [30].

3.4.1 *Morphology Filter*

The morphological filter is useful for this study for polygons and closed features detection, especially in our noisy images. Therefore, I tested the opening-closing operation as pre-processing to suppress noise. The morphology filter of edge detection and smoothing maps the boundaries of homogeneous features in an image based on attributes such as intensity and texture [31]. Morphological filtering simplifies clustered images by smoothing out features boundaries using small sealing gaps and eliminating tiny projections [31]. The dilation operator expands the image features by replacing the pixels with a value of "0" to "1". The opposite operator is called erosion which returns the value from "1" to "0". A combination of the two operators, dilation and erosion, is called closing and opening. Closing is a dilation followed by erosion [31].

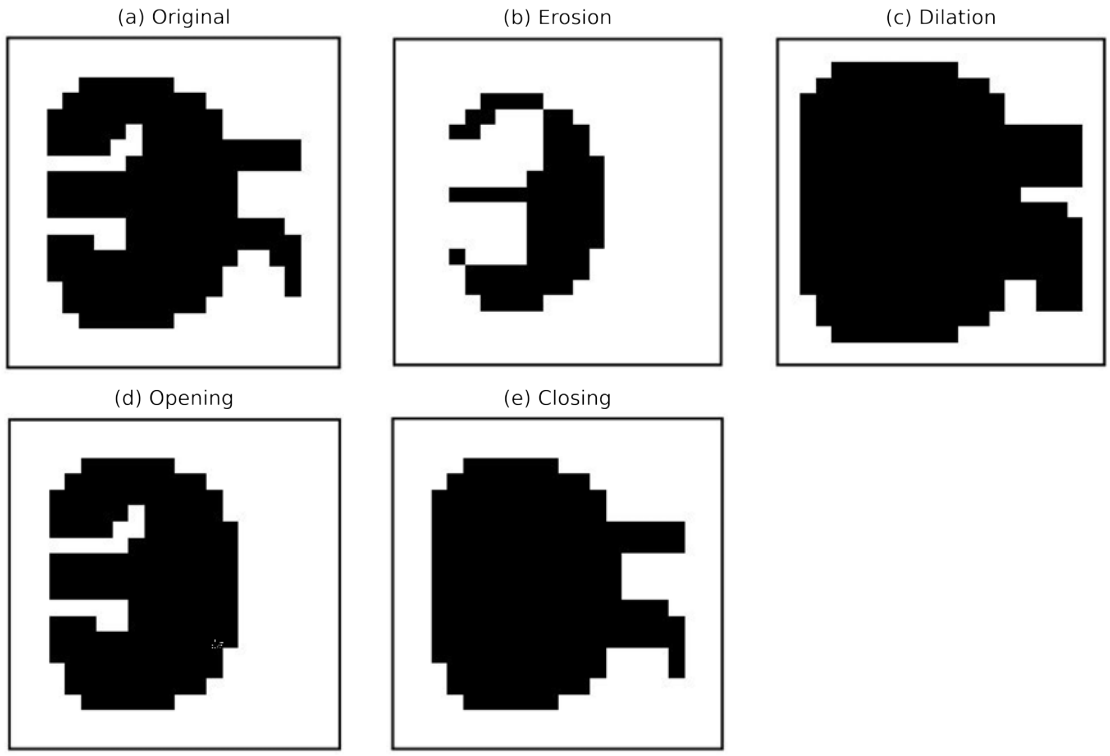

Figure 3.10: Morphology filter effects (a) shows an example binary image. (b) and (c) show how the image is changed by the two most common morphological operations, erosion and dilation. (d) opening is defined as an erosion followed by a dilation. (e) shows the opposite operation of closing (Based on Smith, S. W., 1997).

As per figure 3.10, the effect of the morphology filter differs based on which operator is chosen and whether it is a single operator (erosion - dilation) or combination (opening-closing). In this thesis, I used the opening after testing all techniques to suppress the minor noises resulting after classification as it is more effective and protective to the image pixels.

3.4.2 *Gaussian Filter*

The Gaussian filter has been widely used in image processing and computer vision. However, there are a few issues for using a Gaussian filter for the de-noise purpose as it is smooth, and the signal is also smeared [30].

The two-dimensional digital Gaussian filter can be expressed as:

$$G(x,y) = \frac{1}{\sqrt{2\pi\sigma}} exp\left(\frac{-(x^2+y^2)}{2\sigma^2}\right) \tag{3.4}$$

In equation 3.4 where sigma σ is the standard deviation of the Gaussian kernel and x, y are the distances from the origin in X-axis and Y-axis. Once the kernel is calculated, the convolution with the image is performed. The size of the filter kernel is defined by estimating the 95 percentile of the maximum value of the kernel. Smoothing filters produce distortion and blurring effects to the edges inside images. However, the Gaussian

filter has a more negligible edge distortion effect. The Gaussian filter causes edge position displacement and phantom borders [30].

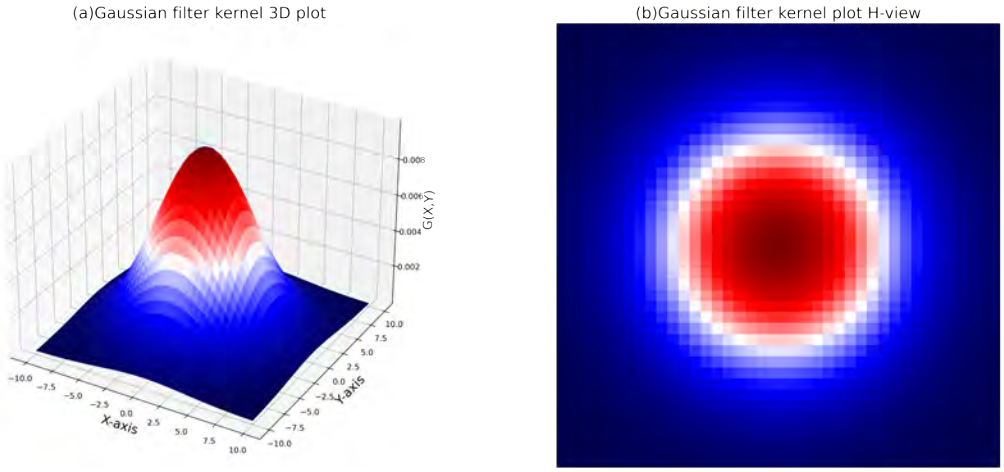

Figure 3.11: Gaussian filter kernel visualization, (a) 3D plot of the Gaussian filter kernel , (b) Horizontal section for the Gaussian filter kernel (exemplary values)

Based on figure 3.11, the Gaussian filter smoothing uses this 2-D distribution as a 'point-spread' function, which is estimated using convolution. The standard deviation plot assumes that the mean is around the point (0,0) and size of kernel is defined by 5 % around the mean. The smoothing is applied to the higher values (red to white colors) and has less to no effect toward the edges of the distribution (blue color 3.11 (b) as per [30]).

The standard deviation value of the Gaussian optimizes the smoothing level by the standard deviation value of the Gaussian. The main Gaussian filter parameter applied in my thesis is the sigma value of 0.2. I used filtering techniques as a pre-processing step before the classification to achieve optimum results.

3.5 ACCURACY ASSESSMENT

The most used thematic maps generated by satellite or remote sensing techniques are a pixel-based classification approaches, and the aerial imagery generated using polygon-based classification approach [32]. My thesis aims to extract all water bodies from other pixels; thus, I wanted to minimize the number of classes to decrease the chances of errors. I tested numbers from 3 to 7 classes, and the adequate number of classes are 3 to 4 classes.

This thematic classified maps require accuracy assessment to validate the efficiency of the approach. In order to evaluate the polygon-based approach, it requires a sample data from the reference data in order to compare it with the classified map. This will be explained in details in the next subsection.

3.5.1 *Confusion Matrix*

It is essential to run the accuracy assessment to validate RGB and NIR classified imagery. The confusion matrices of each output image provide accuracy percentages. Since the ML classification is performed using both supervised and unsupervised classification, the confusion matrices are generated using manual random points via ArcMap software. As per figure 3.12, the manual picked points are created in vector file format and class by class.

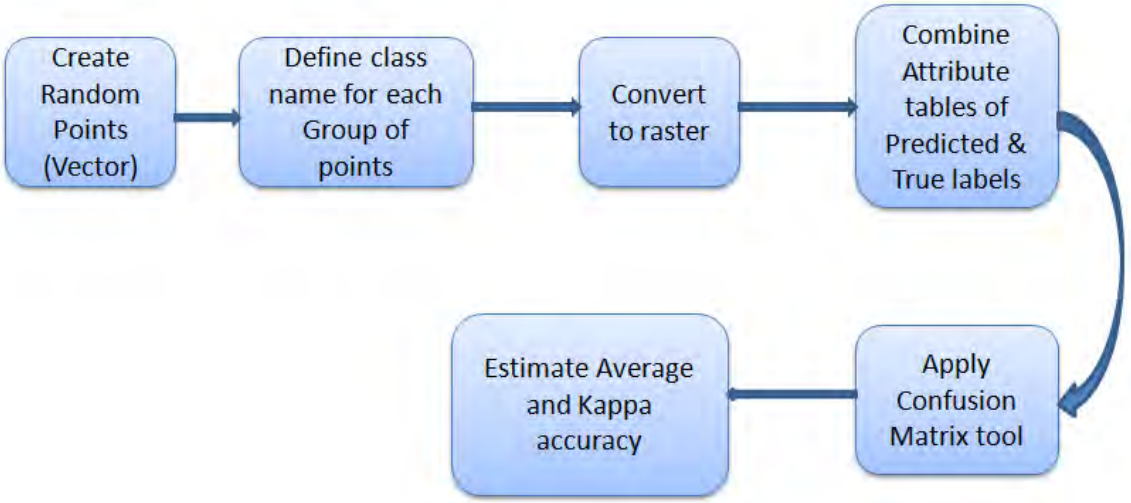

Figure 3.12: Accuracy assessment workflow using ArcMap software

After each class, the class name and number defined in the attribute table are picked. Step 2 consists in converting the actual labels file into raster format (vector to raster tool). Then, the True vs. Predicted table are combined using the Combine tool before executing the Confusion matrix estimation tool. The tables must be identical and have the same labels and ID to avoid error or miscalculations.

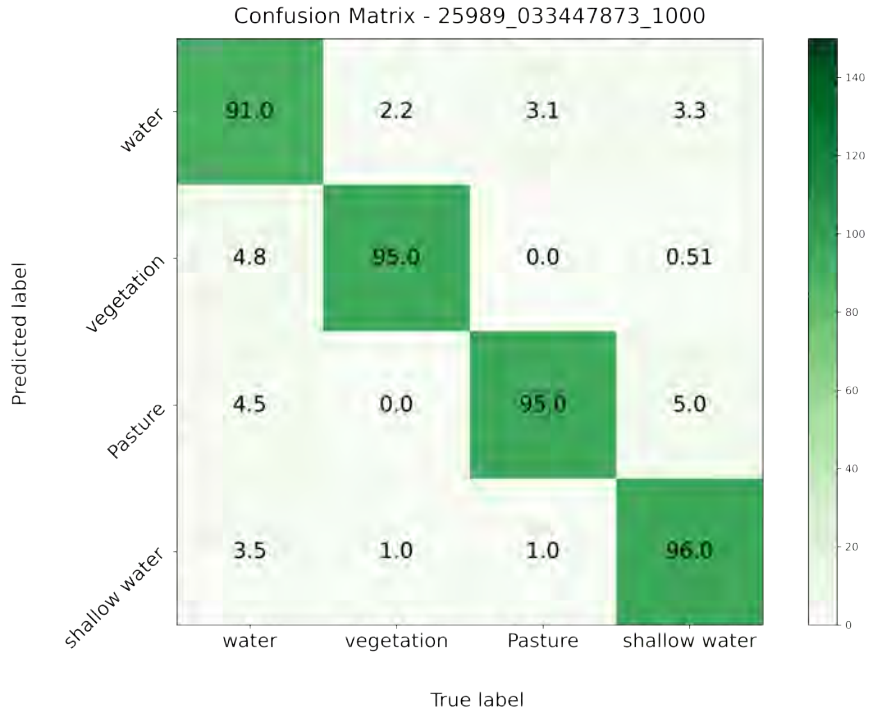

Figure 3.13: Confusion matrix plot of image (25989_033447873_1000) from Teshkpuk west site

As per figure 3.13, the confusion matrix plot of the NIR image from the Teshekpuk west area presents each label's accuracy scores between the true data and predicted (classified) data. The algorithm used for this classification was unsupervised K-means. In this site, we have four classes: water, shallow water, vegetation, and pasture. The true-positive scores, highlighted in dark green, vary from 91% for water to 96% for shallow water. The False-positive values are distributed in the bale green to white cells in the plot.

We also defined a third accuracy: the Kappa accuracy 3.5:

$$K = \frac{p_{agree} - P_{chance}}{1 - P_{chance}} \tag{3.5}$$

Where:

p_{agree} = Proportion of trails in which judges agree.

p_{chance} = Proportion of trails in which agreement would be expected due to chance.

This equation relies on p_{agree}, the trials of the significant match between true and predicted labels, while p_{chance} represents the variance trials between true and predicted labels.

3.5.2 *Validation*

After estimating all accuracy scores in Chapter 3.5.1, the most crucial thing is to correlate the three tested supervised (random forest classification and segment mean shift) and unsupervised (K-means) classification results.

The precision is the ability of the classifier approach not to label as positive a sample that is negative. While the recall is the ability of the classifier to find all the positive samples.

The F-1 score can be interpreted as a weighted harmonic mean of the precision and recall, where an F-1 score reaches its best value at 1 and worst score at 0 (The F-1 scores are normalized values). The three scores together can give more confidence about the best results.

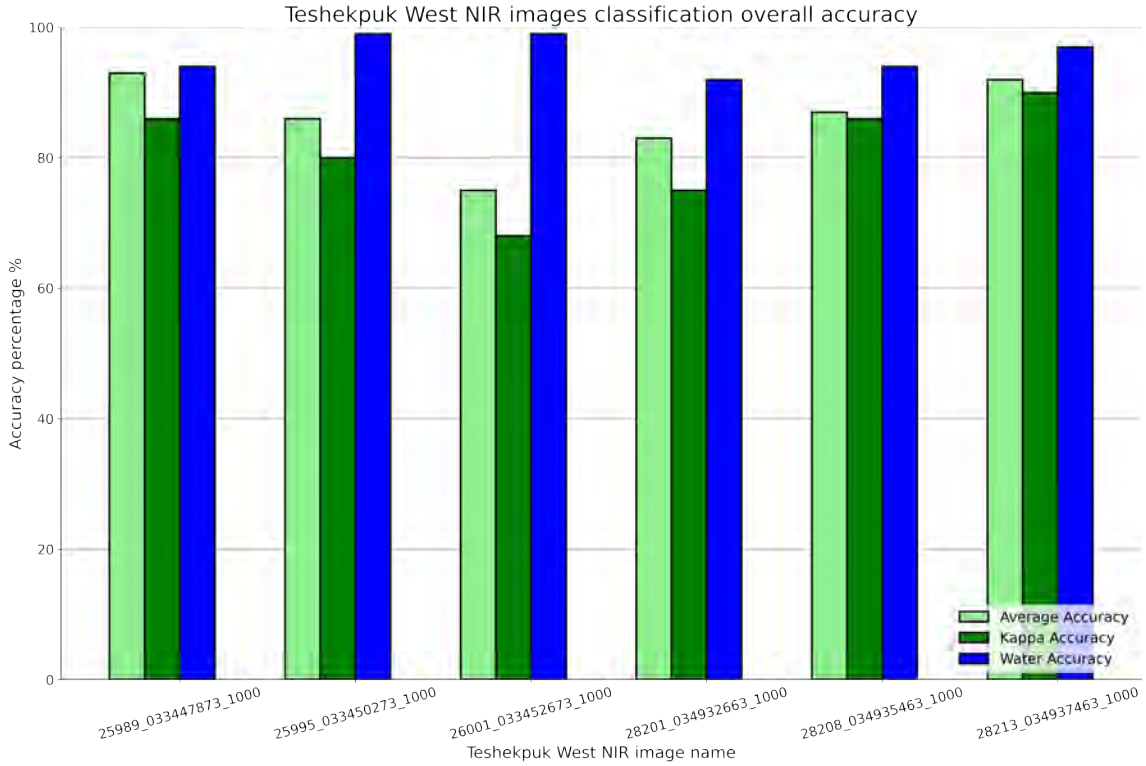

Figure 3.14: Precision accuracy percentage scores for all RGB images of Teshekpuk west (Average - Kappa - Water class)

The Kappa coefficients values were used to estimate the agreement level between two images when compared by the null hypothesis. The null hypothesis states that there is no significant differences between the two images and that the existing differences are due to sampling or experimental error. The average accuracy is estimated by the sum of all true positives divided by the number of classes while the water accuracy is the true positive value of water class only. Kappa statistics values of less than 40% mean poorly performing models, 40–60% are fair, and 60–80% are good. The next step is to validate the accuracy percentage between the ML classification techniques to use the most adapted algorithms.

As per figure 3.14, the Kappa scores for all 6 NIR images vary from 68% to 90%, which is good overall. Since this thesis aims to extract the water bodies from provided aerial imagery, the water class accuracy is used. The water bodies' extraction accuracy varies from 92% to 99%, which is an excellent accuracy score.

3.6 ORTHOMOSAICS MERGING

The final stage is to merge all NIR and RGB images in one scene to represent a meaningful broad terrain. The Orthomosaic is an orthorectified aerial imagery output, generated from a group of images. The imagery color has been balanced to produce an imperceptible mosaic dataset, and the geometric distortion has been suppressed to introduce an exhaustive dataset.

The benefits of aerial remote sensing techniques can be observed when individual images are collected and combined in one wide scene (Orthomosaics); hence some software tools are needed. After capturing the overlapping images, tools such as Agisoft PhotoScan and Pix4Dmapper (Pix4D) are used to stitch them together into a single Orthomosaic image.

In this thesis, The Pix4D is used to generate the Orthomosaics. The production of the Orthomosaic is an automated process with minimum parameterization of the input metafiles and projection of the input images.

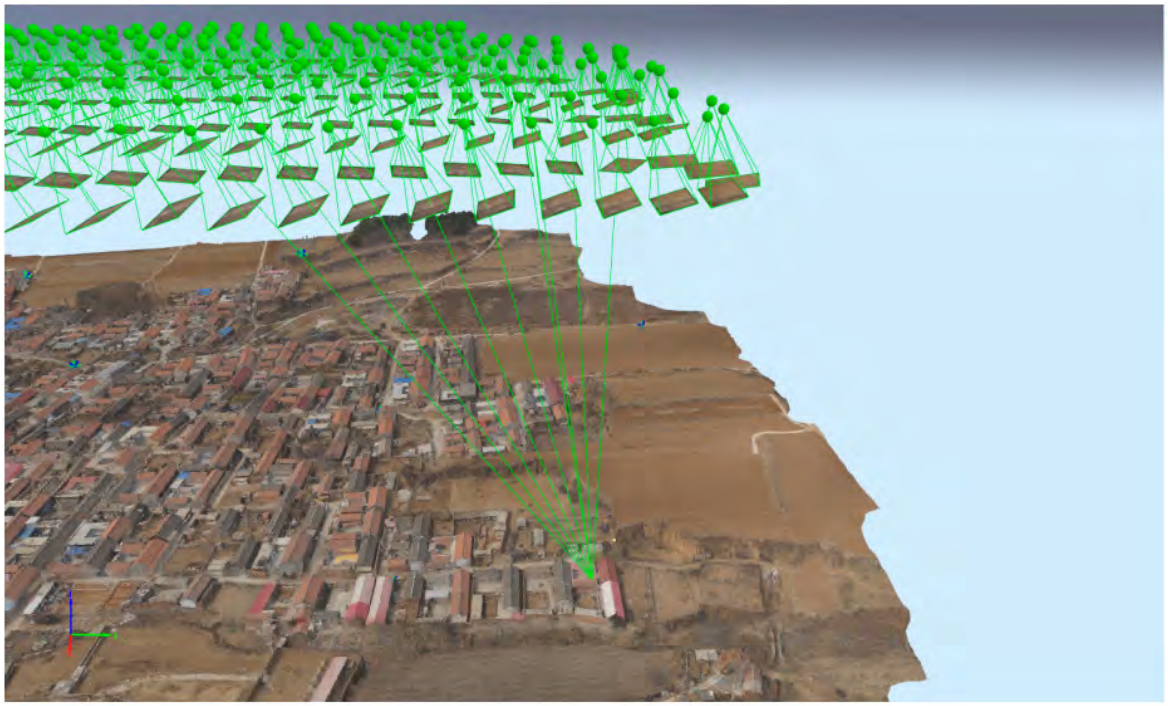

Figure 3.15: UAV drone images illustrate the multi-view of the images (Based on [33])

As per figure 3.15, the camera position and angle are essential for the software to overcome distortion caused by image stitching and color balance. The overlapping is necessary for Orthomosaic preparation. Therefore, the selected user-defined images need to overlap by at least 25%, otherwise, the script will exclude them.

Our images were captured using two cameras for NIR images (right-left) and one camera was used for RGB (Center). With the assistant of Dr. Ingmar Nitze, The Orthomosaics for the three sites (Ikpikpuk - Tesheckpuk - Meade) were produced using an average of 1000 aerial images for each scene. The script used to prepare the datasets is coming from AWI, throughout the AWI GitHub repository (MACS).

(https://github.com/awi-response/MACS_tools/blob/master/Prepare_MACS_Processing.ipynb).

4

RESULTS

4.1 CLASSIFICATION TECHNIQUES VALIDATION

Processing the test images of the study area identified significant differences in water polygons in terms of size, depth, and water bottom vegetation. Therefore, the results tested showed some strengths and weaknesses based on the algorithm, either supervised or unsupervised. For instance, The RGB images of Ikpikpuk have relatively vast water lakes compared to the Meade site since it has many small water polygons. Teshekpuk sites have high centered ice-wedge polygons that provide difficulties to be mapped as they are similar to vegetation pixels response. Therefore, the accuracy scores are checked to give either confidence or rejection of the provided ML methods. The supervised random forest classification is successful with RGB images as the lakes have more marine algae and vegetation, which confuses the algorithm, non-parametric and unsupervised classification.

Based on Chapter 3.5.1, the confusion matrix is estimated for all testing images mentioned in Table 1.1. As per figure 4.3, the resulted average accuracy scores of Ikpikpuk NIR images varies between techniques: the RFC average accuracy scores are between 88-97%, the K-means between 85-94% and the segment mean shift between 81-93%.

The RGB images in figure 4.4 show a higher accuracy range for the supervised random forest classifier compared to supervised segment mean shift and K-means unsupervised classification: the RFC average accuracy scores are between 86-97%, the segment mean shift range is 86-95%, and the K-means range is 82-91%.

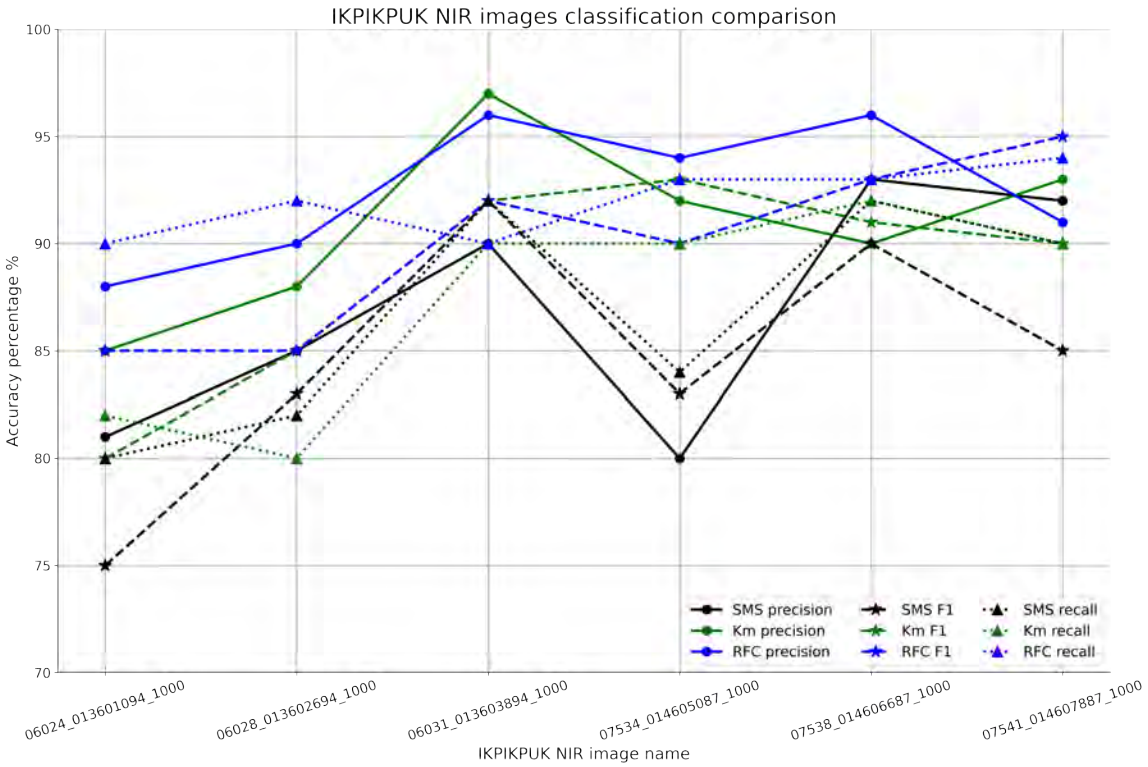

Figure 4.1: Average accuracy scores comparison of ML classification techniques for NIR Ikpikpuk area (RFC: random forest classifier, SMS: segment mean shift and Km: K-means)

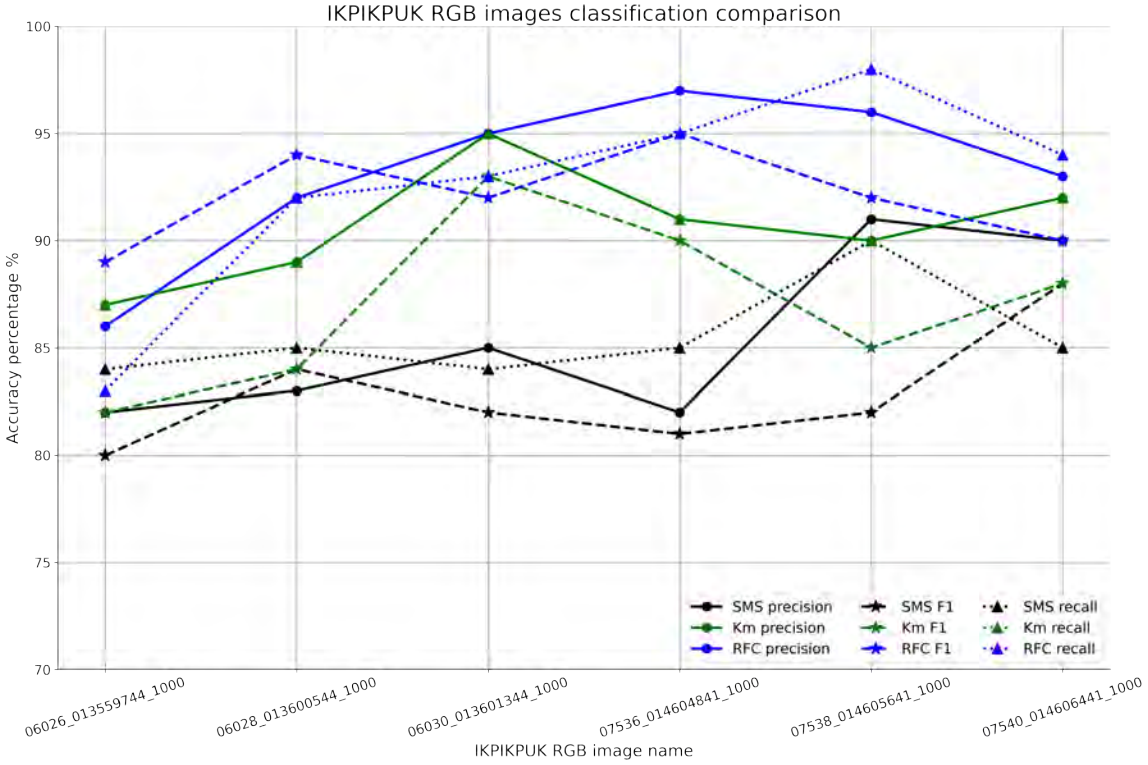

Figure 4.2: Average accuracy scores comparison of ML classification techniques for RGB Ikpikpuk area (RFC: random forest classifier, SMS: segment mean shift and Km: K-means)

In order to validate the success of random forest classification algorithm, I tested it on one of the noisy site images of the Meade site, where there are a lot of shadowing pixels (2.11). The resulting accuracy scores are divided into three types: precision, F1-score and recall (as mentioned in chapter 3.5.2).

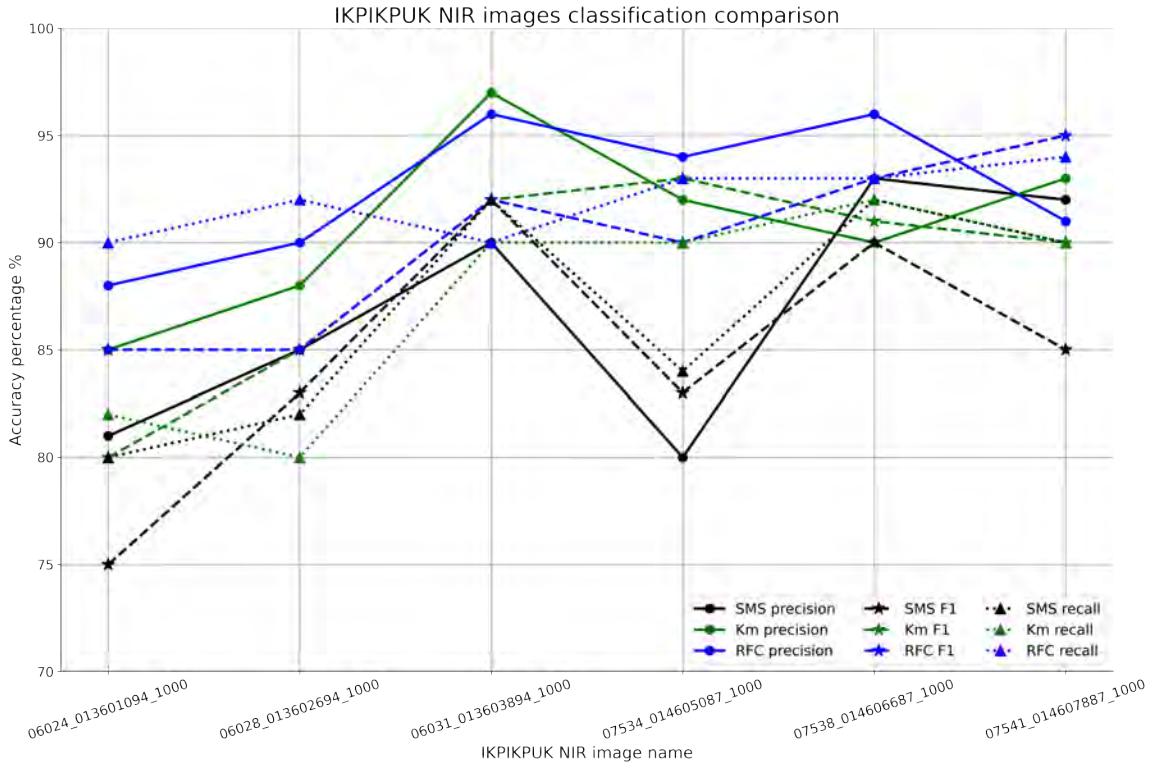

Figure 4.3: Average accuracy scores comparison of ML classification techniques for NIR Ikpikpuk area (RFC: random forest classifier, SMS: segment mean shift and Km: K-means)

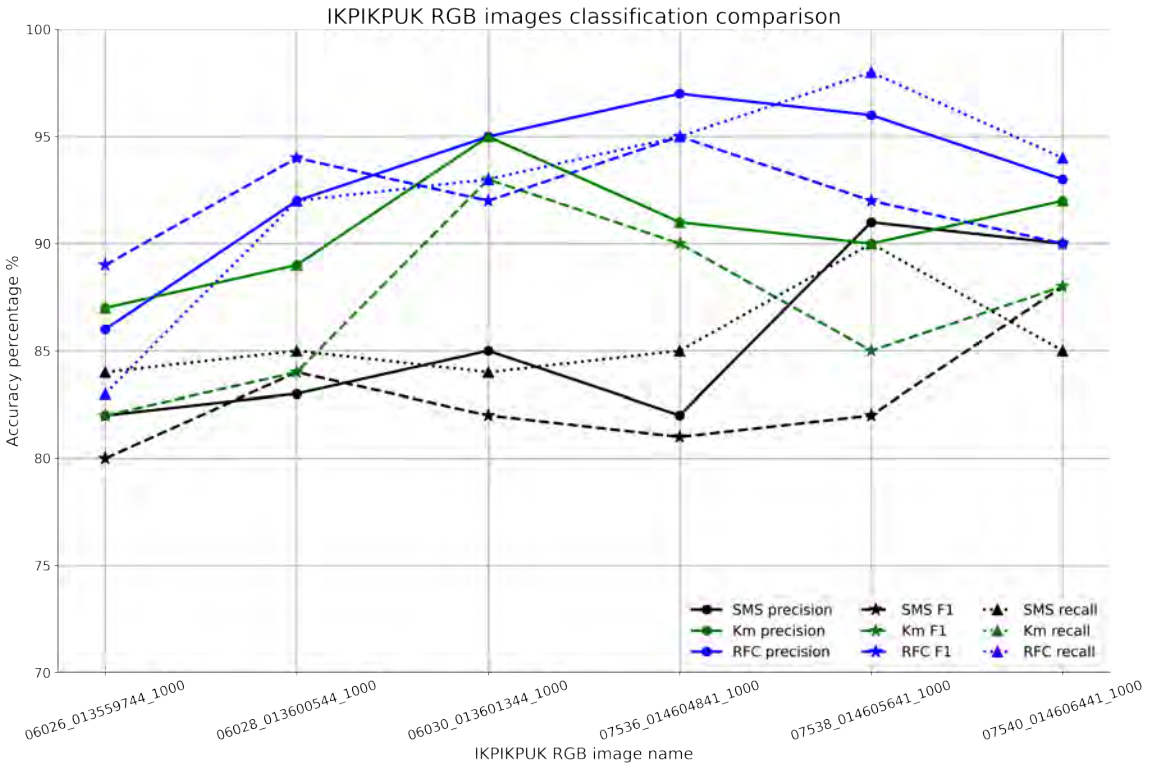

Figure 4.4: Average accuracy scores comparison of ML classification techniques for RGB Ikpikpuk area (RFC: random forest classifier, SMS: segment mean shift and Km: K-means)

As shown in figure 4.5, The NIR images have a high precision accuracy range for SMS (85-92%), , without significant differences between images, while the RFC shows a range of 80-90%, which is close but still less accurate. The Kmeans unsupervised classification scores have proven inadequate for water body extraction, with a precision range of 75-82%.

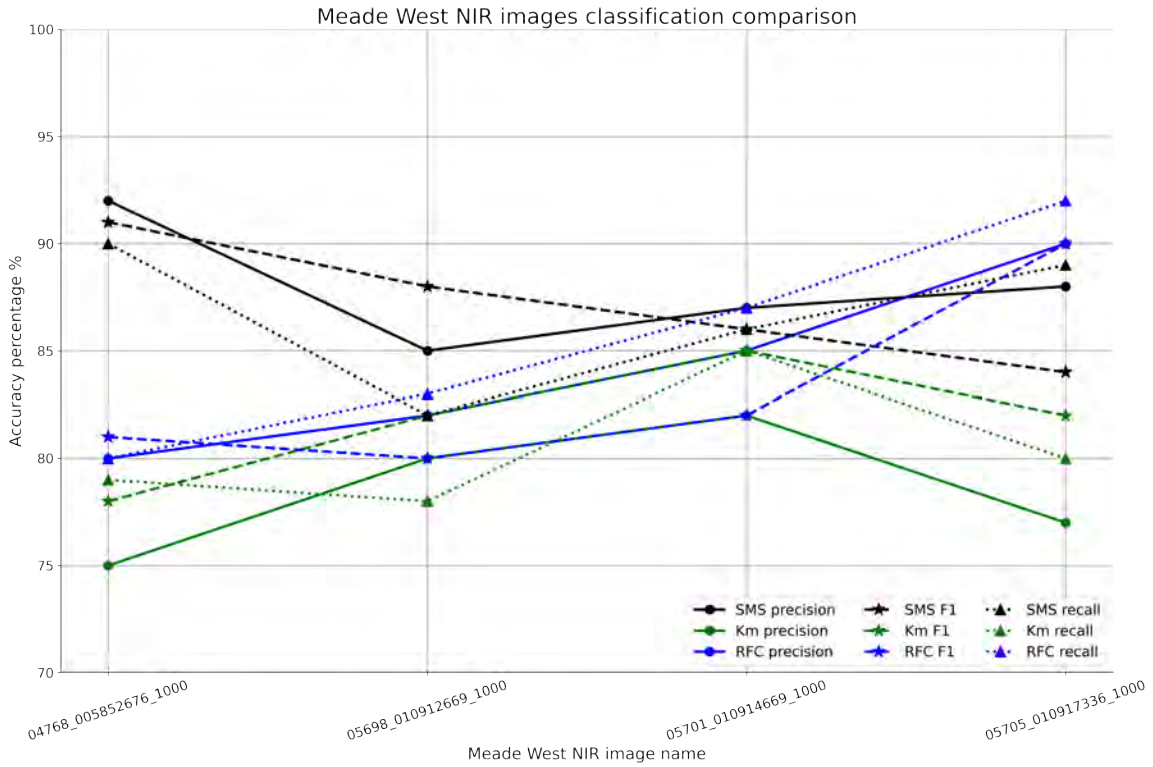

Figure 4.5: Average accuracy scores comparison of ML classification for Meade west NIR images (RFC: random forest classifier, SMS: segment mean shift and Km: K-means)

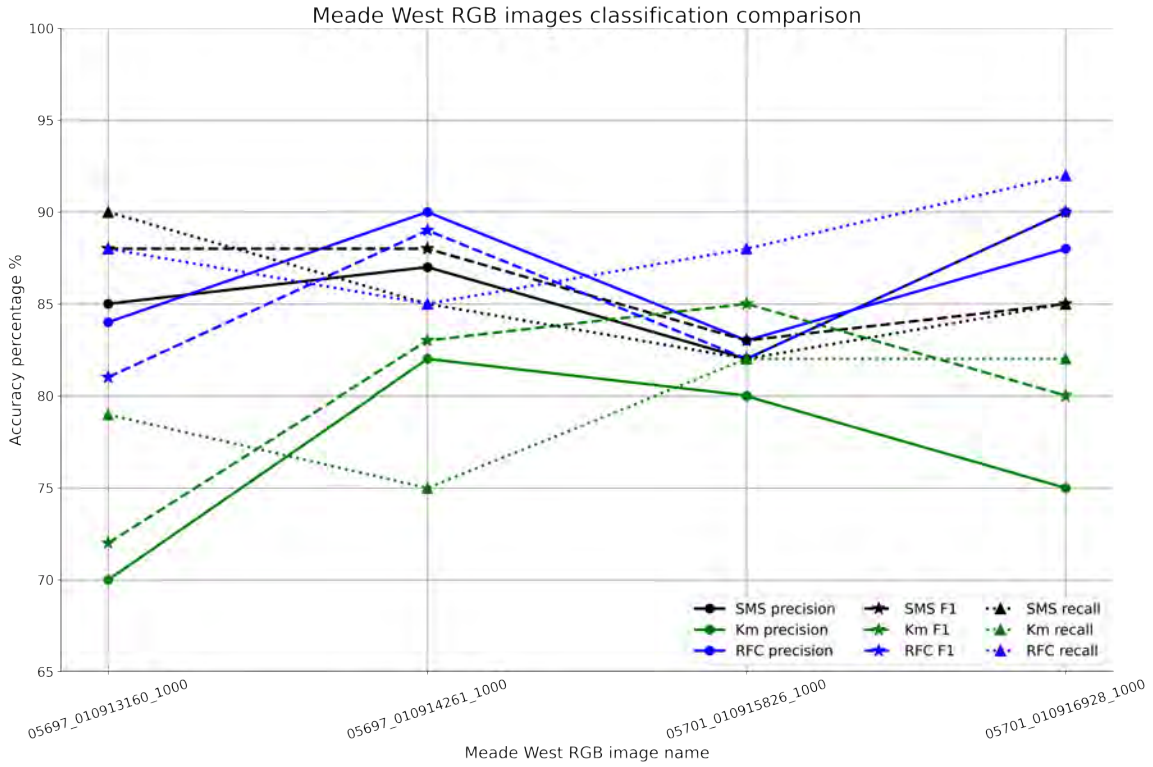

Figure 4.6: Average accuracy scores comparison of ML classification techniques for RGB Ikpikpuk area (RFC: random forest classifier, SMS: segment mean shift and Km: K-means)

However, RGB image classification provided better scores in favour of the supervised RFC figure (4.6). The RFC accuracy assessment precision scores varies between 77-90%, similar to the segment mean shift range of 85 to 90%. The Kmeans classification has low accuracy scores of 70-82%, and thus will not be used in our workflow.

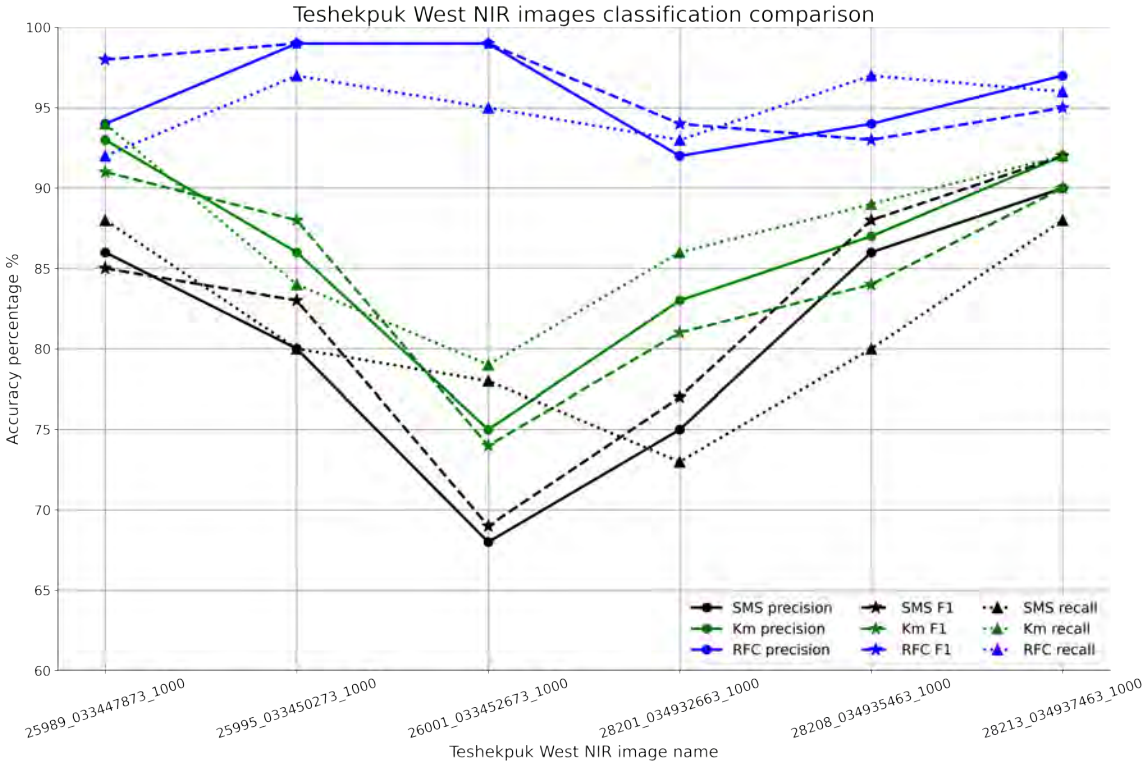

Figure 4.7: Average accuracy scores comparison of ML classification for Teshekpuk west NIR images (RFC: random forest classifier, SMS: segment mean shift and Km: K-means)

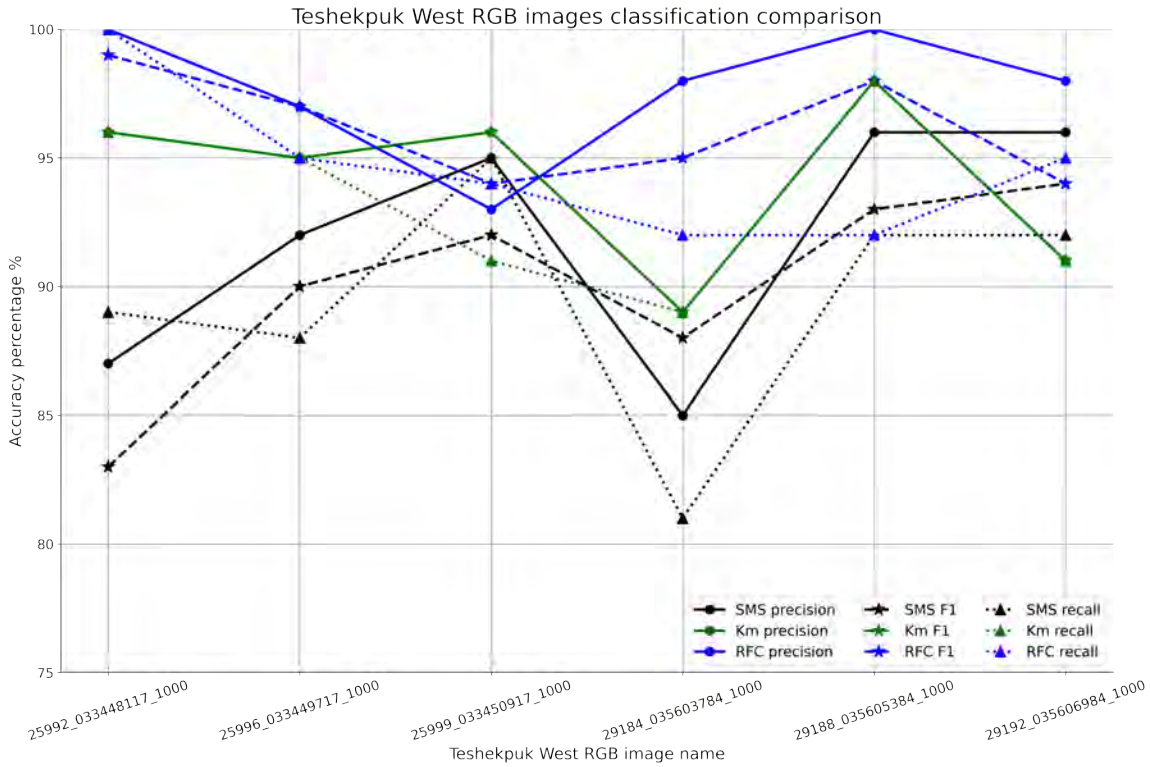

Figure 4.8: Average accuracy scores comparison of ML classification for Teshekpuk west RGB images (RFC: random forest classifier, SMS: segment mean shift and Km: K-means)

On the Teshekpuk site, RGB and NIR image classification shows better scores in favour of the supervised RFC figures (4.8) and (4.7). The RFC accuracy assessment precision scores varies between 93-100%, similar to the segment mean shift range of 83 to 95%. The Kmeans classification has low accuracy scores of 72-92%, and thus will not be used in our workflow as per all previous scores.

The average accuracy percentage shows relatively fewer differences as it was built mainly based on random points (about 150 - 200 points), while the primary reference to judge the success of each technique is to always compare visually by eye with input images. The relation between precision, F-1 score, and recall is inconsistent in terms of differences between each one for the same image; however the overall accuracy scores vote in favor of RFC workflow (figures from 4.3 to 4.8).

4.2 IKPIKPUK DELTA ORTHOMOSAIC CLASSIFICATION VISUALISATION

The accuracy scores for the three different classification methods, random forest classification, K-means, and segment mean shift as per figures from 4.3 to 4.8 , show that RFC is overall successful in RGB and NIR classification. The next step is to validate the RFC classification in detail, especially to detect the water bodies.

The random forest classification algorithm was performed using a training sample of 4 class labels: water, vegetation, shallow water, and pasture. Chapter 1.2 (Thesis outline) states that the workflow has a Gaussian filter applied pre-classification to filter out the noise and minor distortions. Besides, the opening morphology filter is applied to the labels since the RGB bands show more unwanted details.

As per figure 4.9, The Ikpikpuk input RGB Orthomosaic shows a stripping effect from the illumination of the image swaths, and this is the best Orthomosaic result. There is also a gap in the middle of the lake due to missing images and less overlap. As mentioned in Chapter 3.6, the script will exclude the images with no overlap. Therefore, it was necessary to apply a mask to remove the missing data areas from the classified output in figure 4.9 (b). The main goal is to extract the water bodies, and there is complexity as shallow water areas appear with different reflectance values.

This is why two classes are designed to separate the deep clear water area from the shallow water area. The results, in general, follow the same significant trends of the RGB Orthomosaic. However, the small water polygons are less accurate and could not be adequately mapped compared to NIR results in figure 4.11 and 4.12.

(a) Input RGB Ikpikpuk Orthomosaic

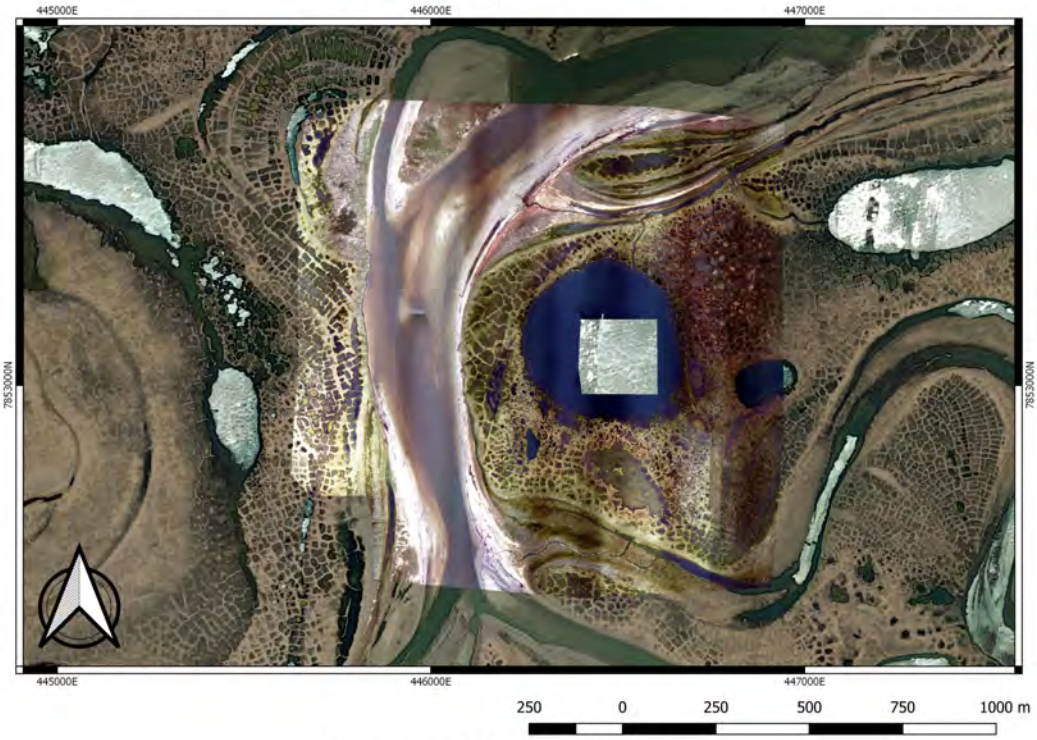

(b) Classified RGB Ikpikpuk Orthomosaic

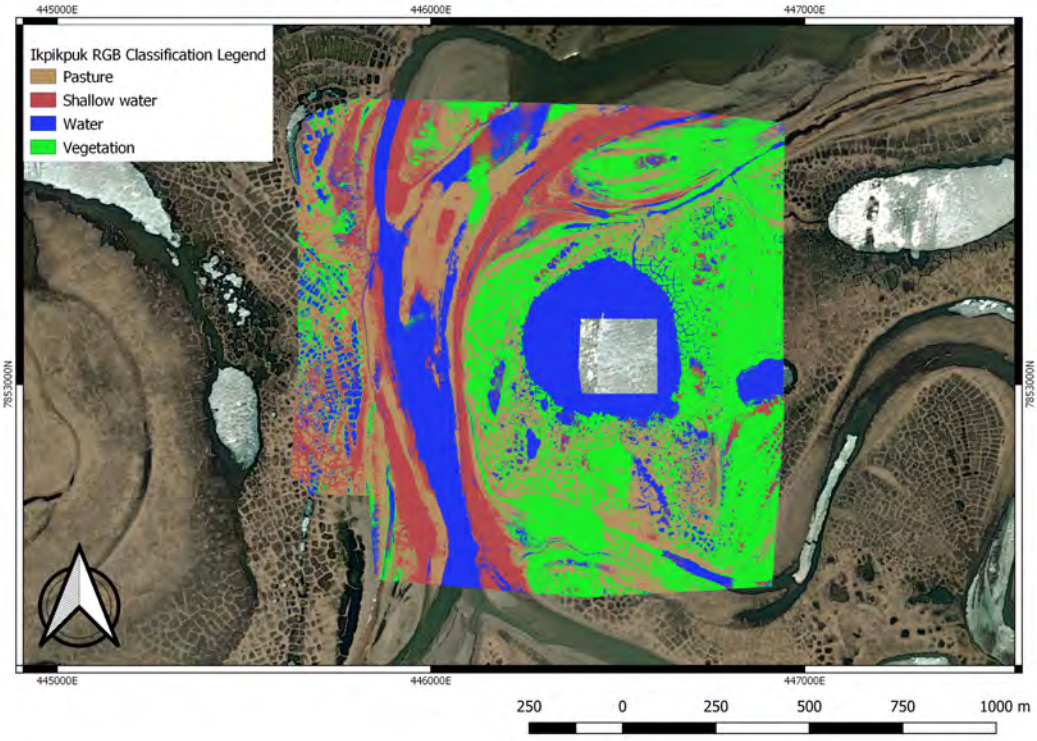

Figure 4.9: Comparison between (a) Input Ikpikpuk RGB Orthomosaic data, (b) RFC Ikpikpuk datasets (4 Classes)

(a) Input RGB Ikpikpuk Orthomosaic (Zoom)

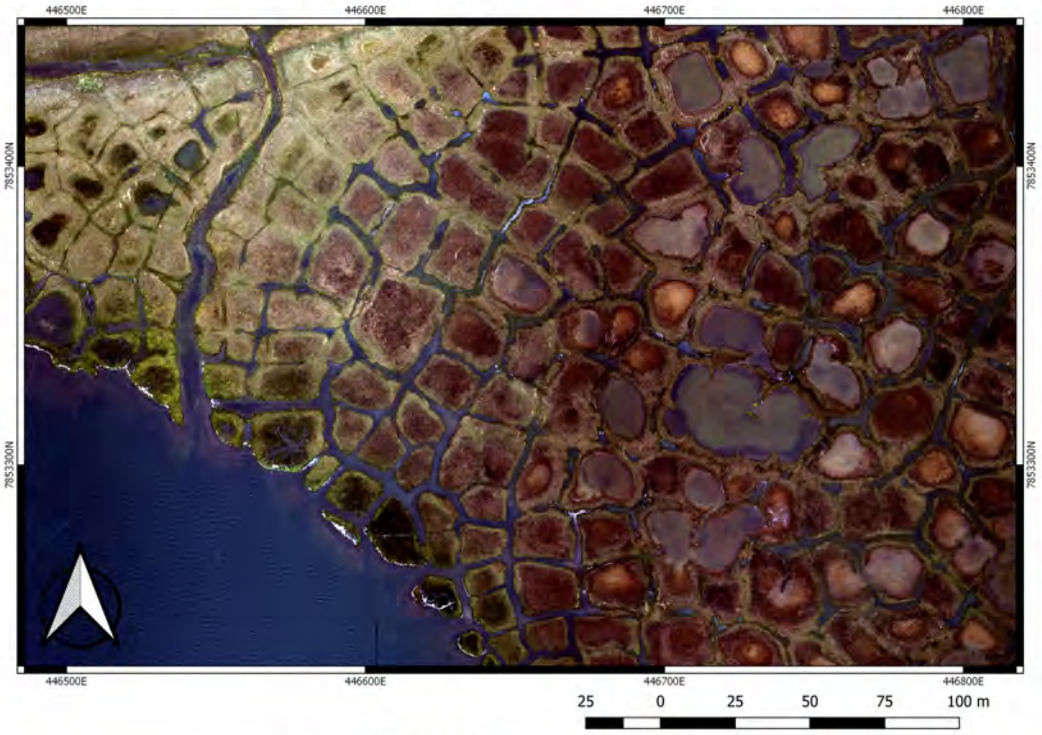

(b) Classified RGB Ikpikpuk Orthomosaic (Zoom)

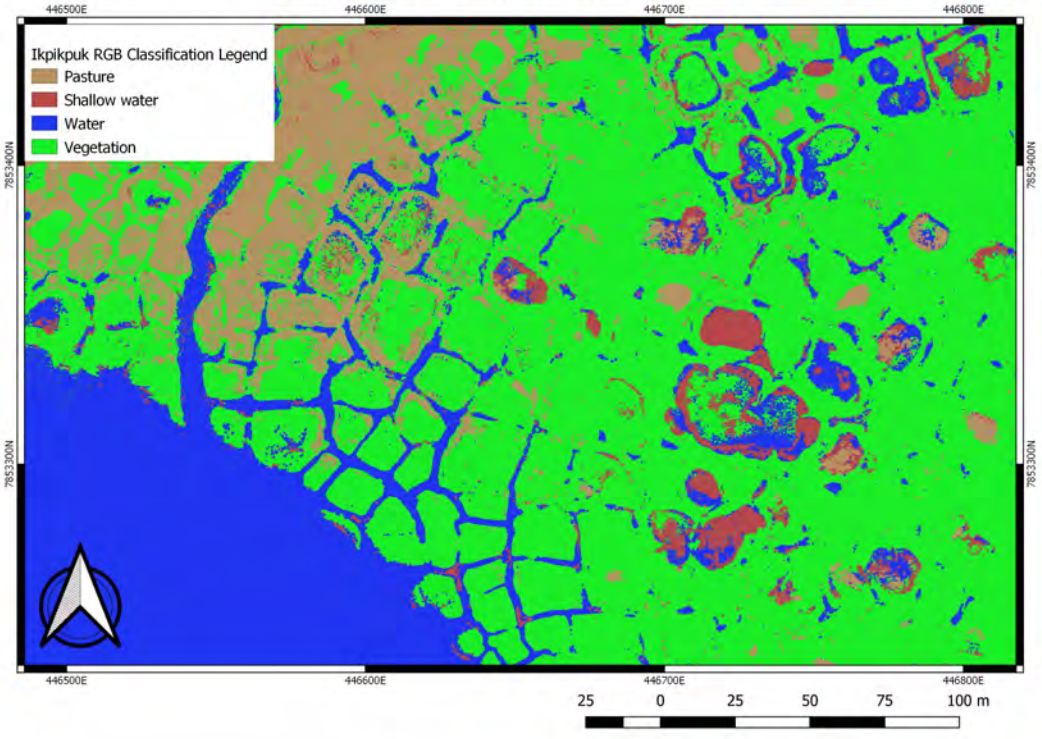

Figure 4.10: Comparison between (a) Input Ikpikpuk RGB Orthomosaic data, (b) RFC Ikpikpuk datasets (4 Classes)(zoomed)

However, the Ikpikpuk NIR Orthomosaic has minor terrain detail and a more significant appearance of the water bodies. NIR infrared images allow clear water bodies visualisation because water surfaces absorb other short wavelength bands.

As per figure 4.11 and 4.12, The first image 4.11 (a) shows the NIR Orthomosaic, and it has more visible dark surface due to water bodies. Compared to RGB, NIR Orthomosaic displays fewer subsurface details, leading to more stable classification results than for RGB as per figures 4.9 and 4.10. As NIR has fewer details, creating a training sample file with three classes is convenient. The zoomed display show the good accuracy to map water bodies among the other classes 4.12.

In conclusion the user has the choice between using NIR, where water bodies are easier identified than in RGB images, or used RGB images, but in that case it is very important to apply Gaussian and Morphology filters in order to remove outlier and noisy pixels even if this comes at the cost of low resolution. The shallow water surfaces have blurry edges due to the application of the morphology and Gaussian fliter, it is a side effect expected and accepted to have more significant results (as mentioned in chapter 3.4).

Overall, the RFC results are acceptable visually and statistically compared to other tested techniques.

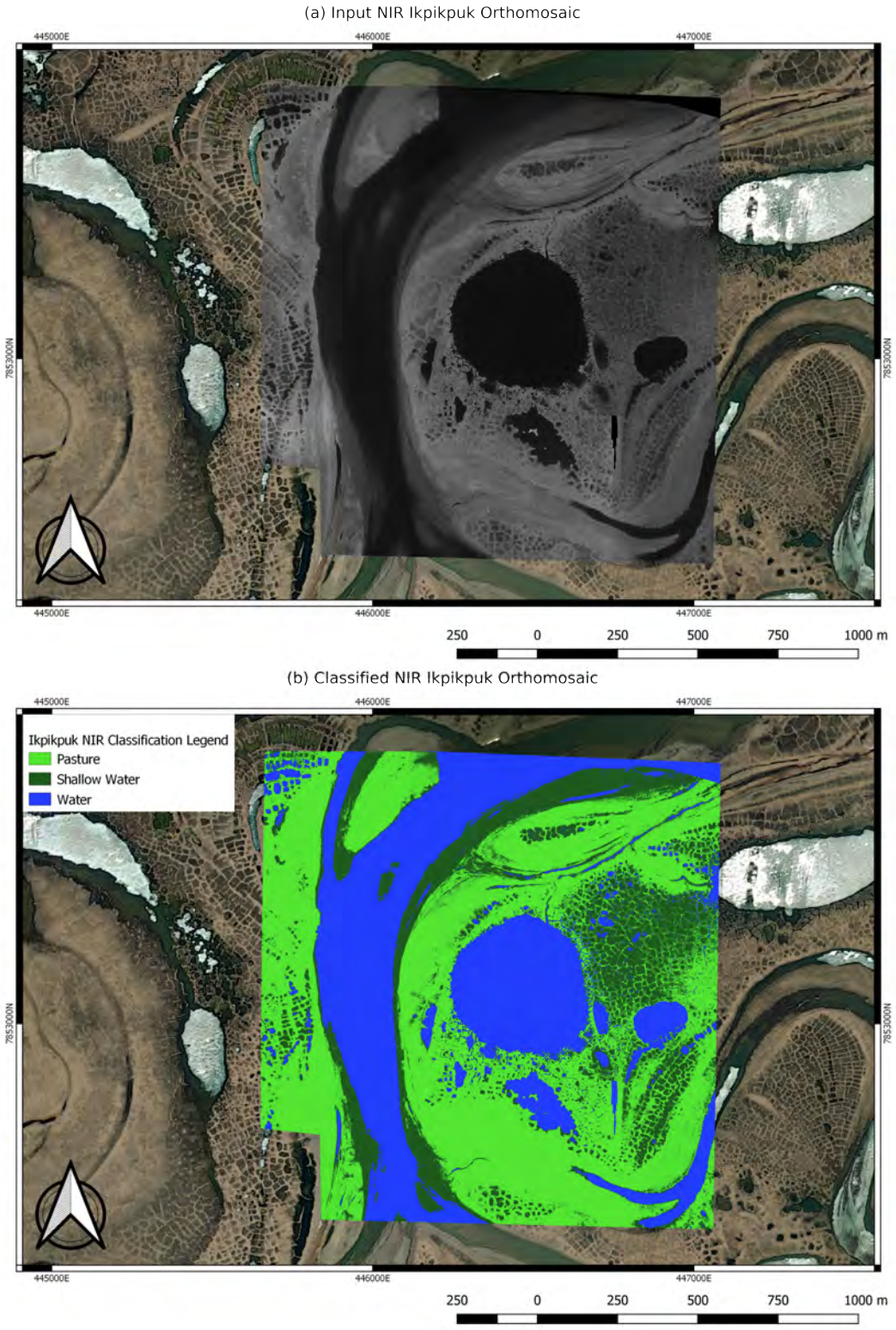

Figure 4.11: Comparison between (a) Input Ikpikpuk NIR Orthomosaic data, (b) RFC Ikpikpuk datasets (3 Classes)

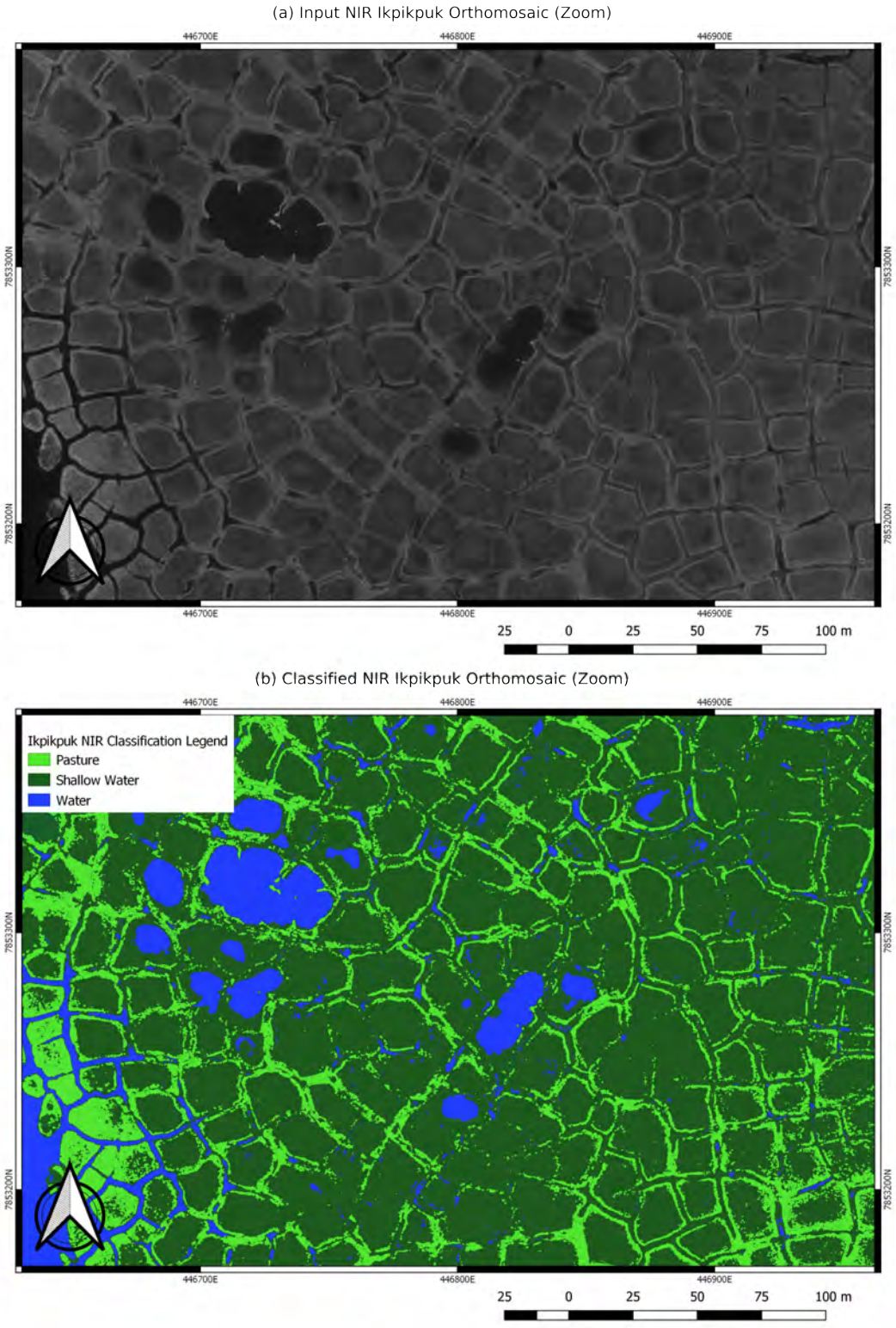

Figure 4.12: Comparison between (a) Input Ikpikpuk NIR Orthomosaic data, (b) RFC Ikpikpuk datasets (3 Classes)(zoomed)

5

DISCUSSION

5.1 MEADE AREA DIFFICULTIES

The aerial photo of figure 2.11 in Chapter 2.1.3 represents the distribution of vegetation that causes shadowing toward the opposite direction of the sunlight. Therefore, the Meade site is complicated as the reflectance is distorted and classifications provide relatively different responses as figure 5.1.

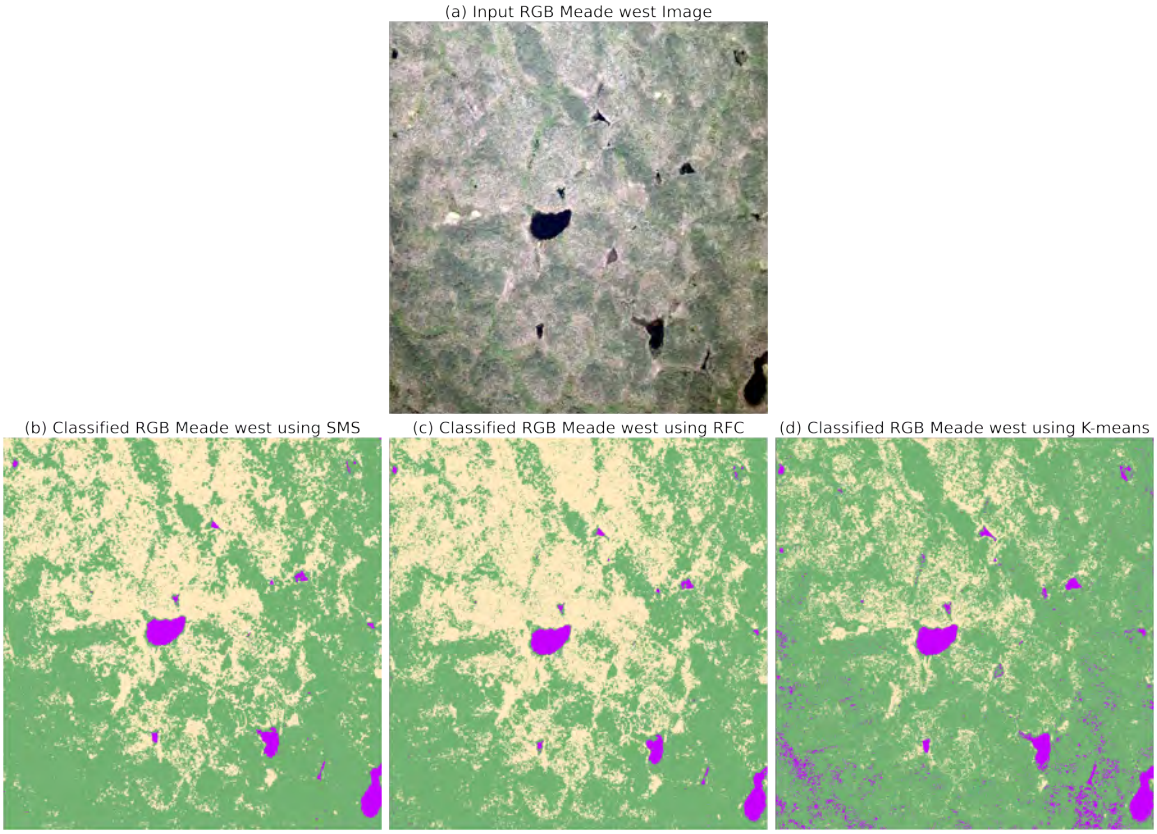

Figure 5.1: ML supervised/unsupervised classification quality comparison, (a) The input RGB image of Meade west catchment, (b) classification results after segment mean shift, (c) classification after supervised random forest classifier result, (d) classified image using unsupervised K-mean.

The figure shows how difficult it is to differentiate between the vegetation classes. Also, there are false water-labelled pixels due to the shadowing effect of the tundra leaves.

The unsupervised K-means has a lot of misinterpreted pixels in purple colour, which represent the water label. The non-parametric clustering leads to better mapping of the small lakes. However, the tundra vegetation has less quality with noisy disseminated pixels, which cannot be filtered with no distortion.

The next step is to check the quality assessment scores of the water body class accuracy, average accuracy score, and Kappa accuracy score. In figure 5.2, the accuracy scores represent the average accuracy (light green color), and it is the highest among the Water class scores and Kappa coefficient. The average accuracy score varies from 80-100% against 75-100% for the Kappa one. Meade west provides, in general, lower accuracy scores as it has small lakes and water bodies compared to the east.

(a) Meade East RGB accuracy

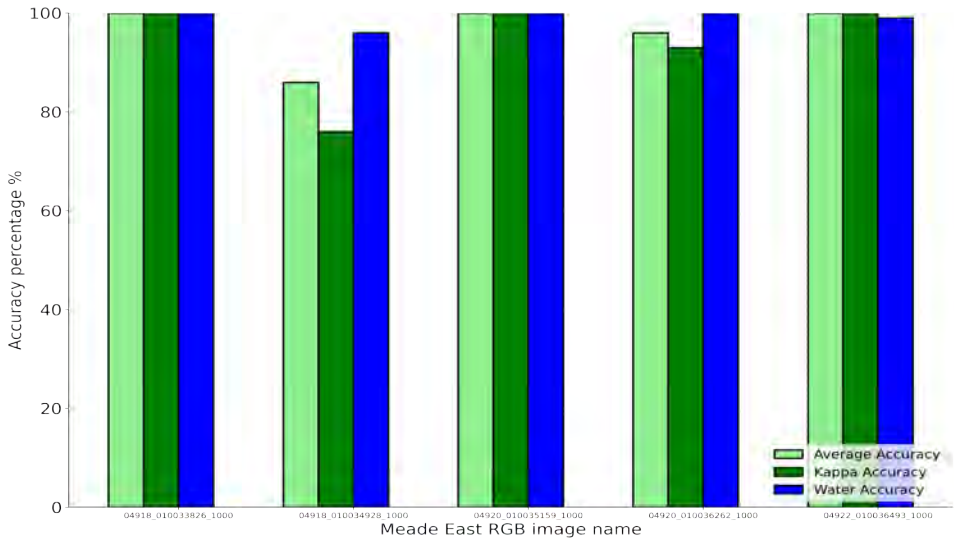

(b) Meade West RGB accuracy

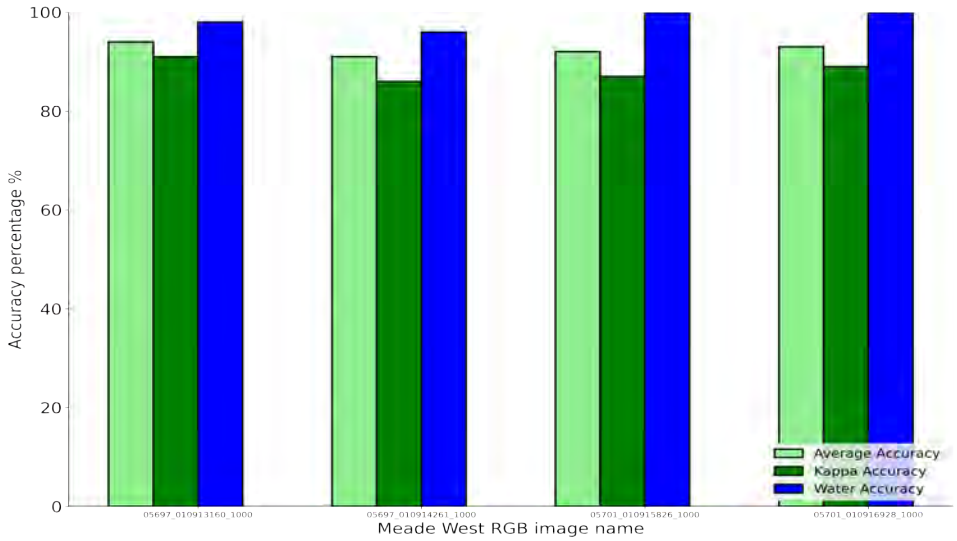

Figure 5.2: Meade area RGB test images Confusion matrix precision accuracy scores for Average accuracy (light green), Kappa accuracy (green) and Water class accuracy (blue), for (a) Meade East, (b) Meade West

5.2 DOWN-SAMPLE OF THE ORTHOMOSAICS

The average number of aerial imagery used for one Orthomosaic was 1000 images, and each image contained around 3000x4000 pixels. Therefore, the resulting Orthomosaic will be too heavy for PC memory and processors. Thus, we needed to downsample the data to save memory while maintaining the Orthomosaic quality. Splitting the data was unsuc-

cessful as the overlapping is essential for the algorithm's clustering precision. Thus we downsampled the orthomosaics 5 times. It was possible because the number of images used and pixels per image were sufficient to preserve the topography and resolution.

5.3 DENOISE FILTERS

In the automated RFC workflow, there were two passes of denoise. The Gaussian filter was tested pre and post-classification and showed more stability to be applied before using sigma = 0.2. The standard deviation varies based on the complexity and topology of the input data; however, it is recommended to keep sigma between $0.2 \leq \sigma \leq 0.75$ to keep the majority of the data features. Testing sigma using another value became too severe to the data quality for this study but could provide adapted results for other data.

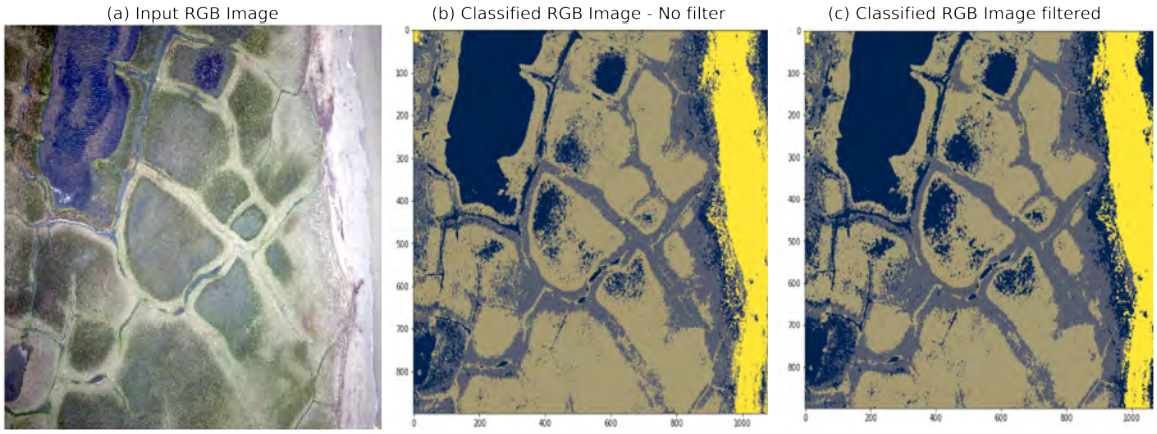

Figure 5.3: Ikpikpuk RGB test image with (b) RFC classified image without denoise (c) RFC classified and denoise image

The other filter was the morphology filter, using the opening combination method. Since the main target is to extract water bodies, the opening approach aims to preserve the dark pixels and expand them while closing can work against the primary goal of this thesis. As per figure 5.3, the classified image using filter (figure 5.3 (c)) has more significant ice-wedge polygons and is more visible than the unfiltered image (figure 5.3 (b)). There are also minor noisy pixels inside the lakes suppressed by the de-noise filters.

6

CONCLUSION

The observation to water bodies continuously is essentail to study the global warming hazards to permafrost regions. I used remote sensing aerial photogrammetry both NIR and RGB to classify water bodies using ML supervised and unsupervised techniques and looking at all the results in the previous chapters shows there is no approach that is working perfectly but the models are acceptable visually.

In conclusion, there is no one unique successful model to be used for all aerial remote sensing photogrammetry as the accuracy scores vary from one area to another based on the complexity of the near-surface feature and reflectively (figures A.2, 5.2 and 4.3 to 4.6).

The supervised random forest classifier has most control over the resulting quality since you have the freedom to select the number of classes and the training data that will be used to guide the algorithm. Nevertheless, the computation can be heavy if the spatial resolution is high (small pixel size) and the number of pixels is high. Thus, supervised segment mean shift classification can be more beneficial if the input Orthomosaics are NIR images, as these images have more clarity for water bodies mapping. The other proposed solution is to down-sample the data, while keeping a sufficient quality, to save some memory to run the supervised random forest classification.

The application of Gaussian filter with proposed sigma value as mentioned in sections 3.4 can be very useful to clean the data prior to classification. Nevertheless, in my thesis, post-classification leads to smeared data but it can be helpful in other datasets. The morphology filter enhances the quality of the classified maps and increased the SNR ratio in adequate levels as per figure 5.3.

In conclusion, I recommend the supervised random forest classification for water bodies extraction purposes in RGB and NIR images. I believe that different data nature and other weather conditions can provide more insights into the best-automated machine learning algorithm and validate or disapprove my research outcome.

A

APPENDIX

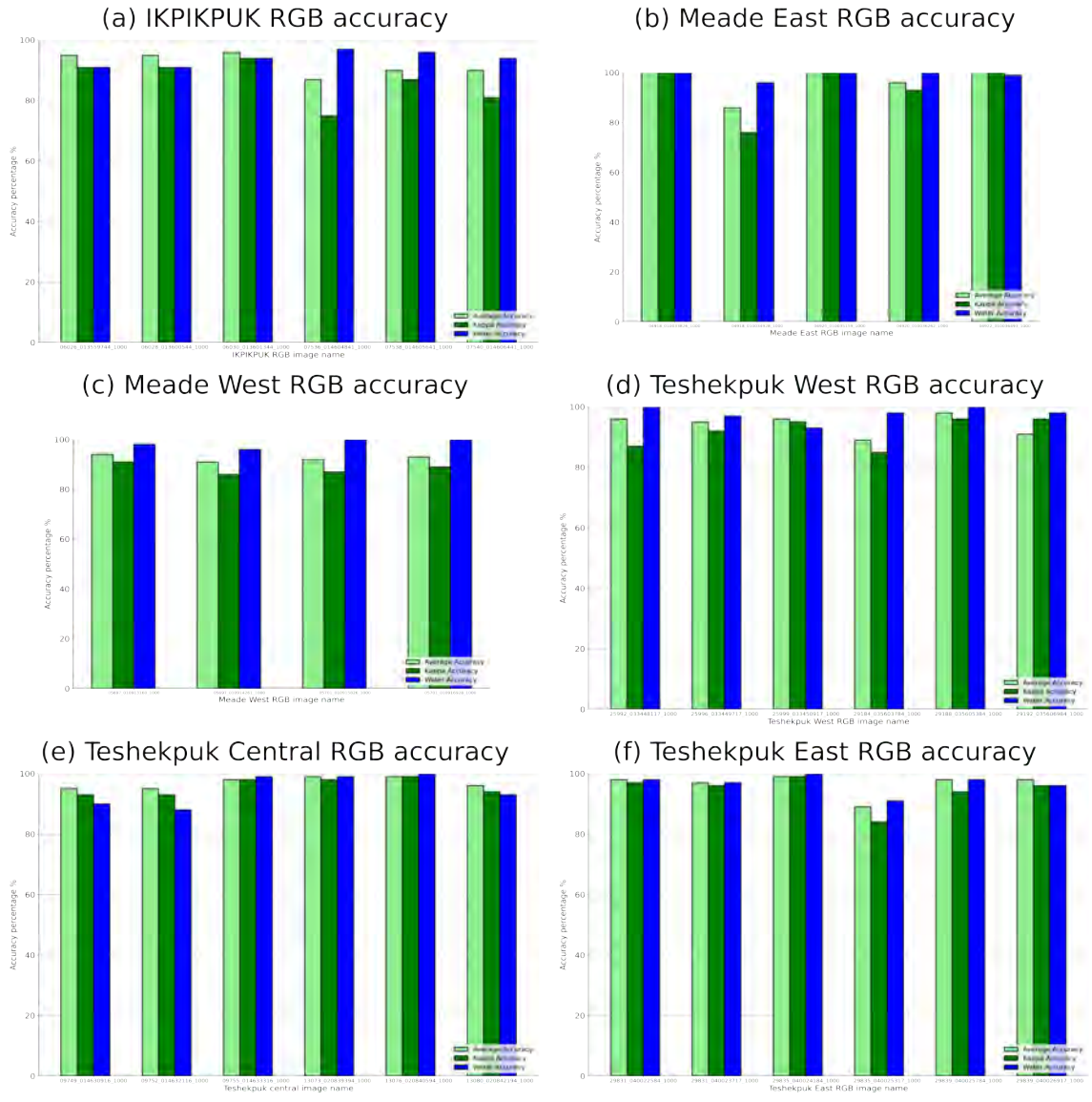

Figure A.1: RGB test images Confusion matrix accuracy scores for Average accuracy (light green), Kappa accuracy (green) and Water class accuracy (blue), for (a) Ipikpuk, (b) Meade East, (c) Meade West, (d) Teshekpuk West, (e) Teshekpuk Central, (f) Teshekpuk East

(a) Input RGB Tesheckpuk East Orthomosaic

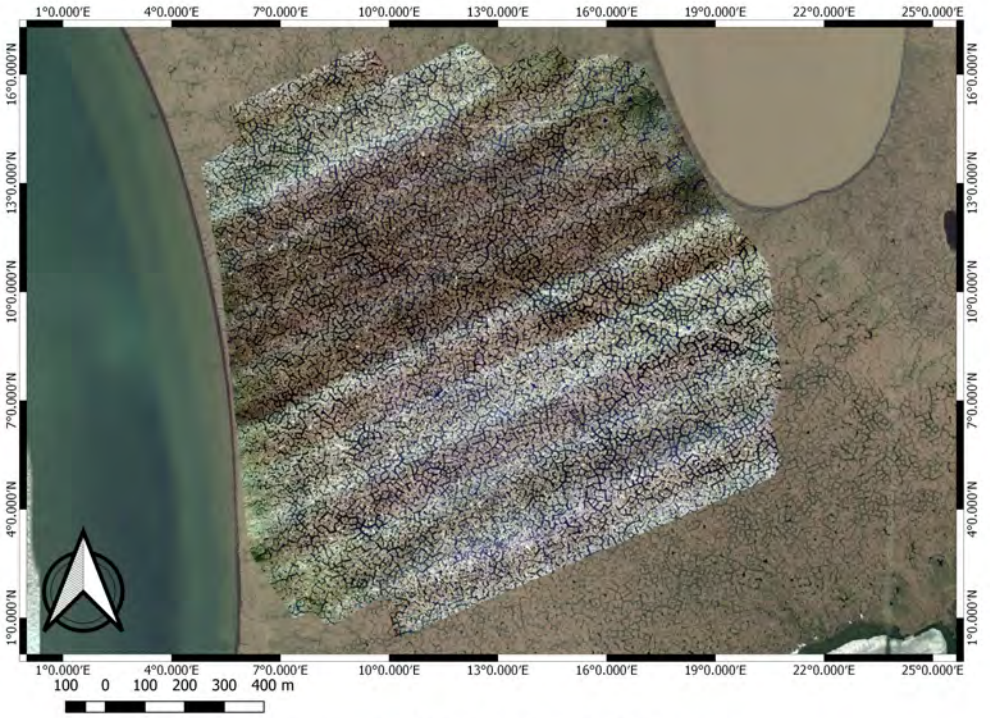

(b) Classified RGB Tesheckpuk East Orthomosaic

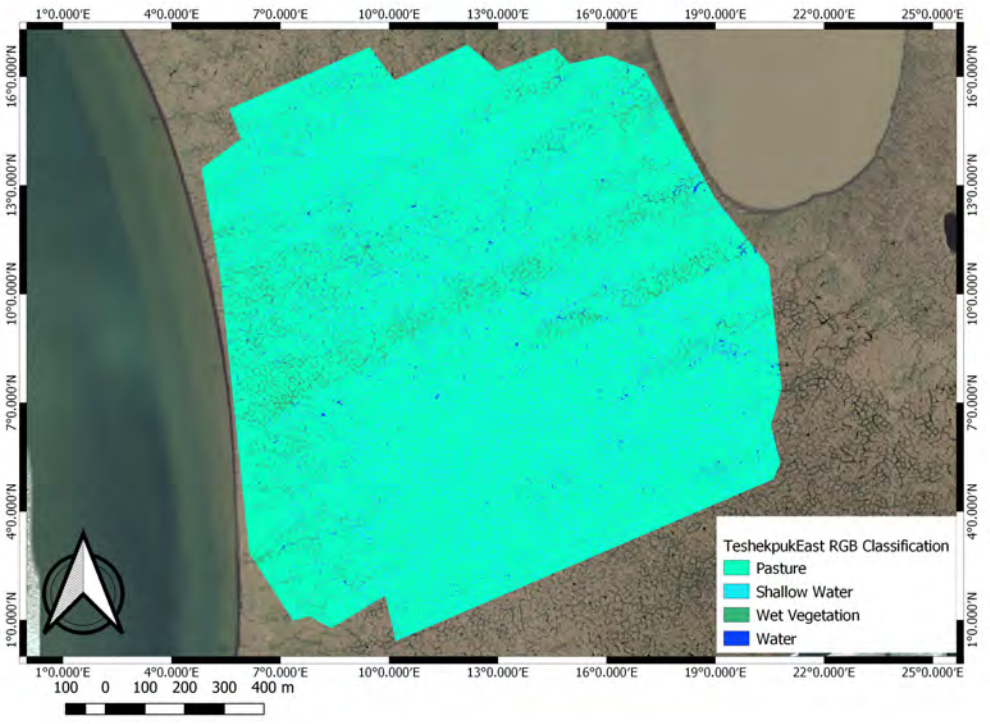

Figure A.2: Comparison between (a) Input Tesheckpuk East RGB Orthomosaic data, (b) RFC Tesheckpuk East datasets (4 classes)

Scripts for this thesis:

https://github.com/Abdelwahab86/Water-polygons-photogrammetry.git

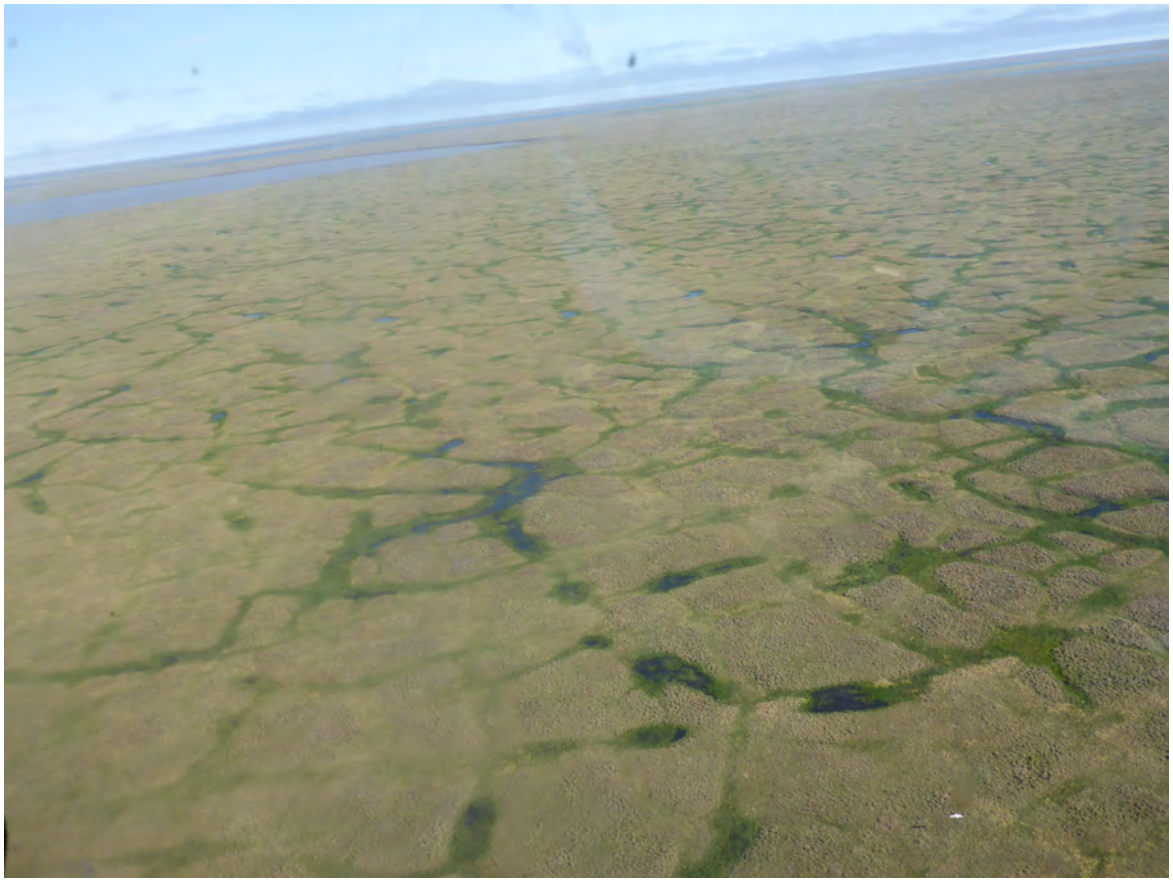

Figure A.3: Photo for Teschekpuk East for Tundra vegetation (taken by Thaw Trend Air 2019 flight campaign)

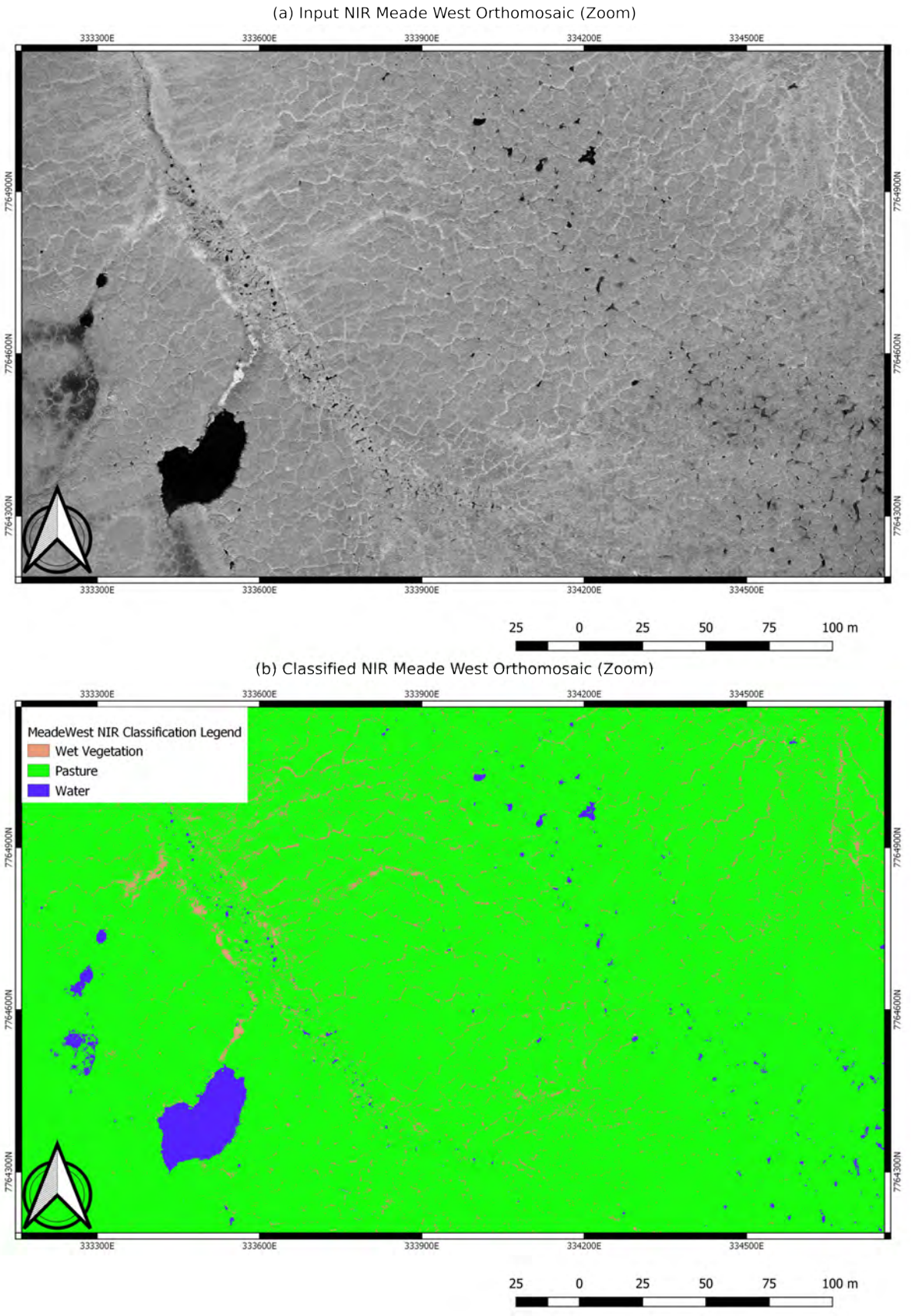

Figure A.4: Comparison between (a) Input Meade West NIR Orthomosaic data, (b) RFC Meade West datasets (3 classes)(zoomed)

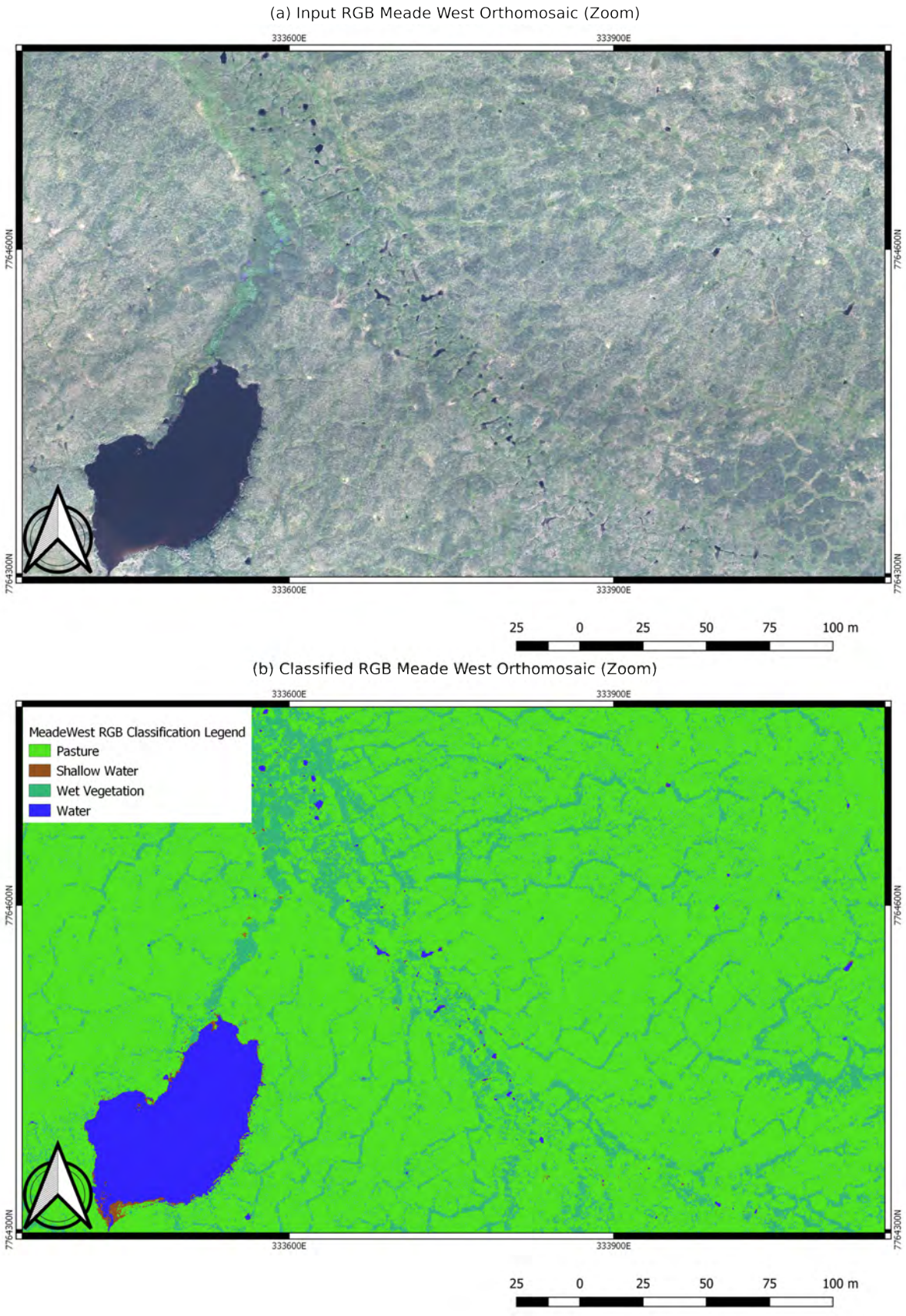

Figure A.5: Comparison between (a) Input Meade West RGB Orthomosaic data, (b) RFC Meade West datasets (4 classes)(zoomed)

BIBLIOGRAPHY

[1] R. J. E. Brown, 'The distribution of permafrost and its relation to air temperature in canada and the u. s. s. r.', *Arctic*, vol. 13, no. 3, pp. 163–177, 1960, ISSN: 00040843. [Online]. Available: http://www.jstor.org/stable/40506998.

[2] I. Nitze, G. Grosse, B. M. Jones, C. D. Arp, M. Ulrich, A. Fedorov and A. Veremeeva, 'Landsat-based trend analysis of lake dynamics across northern permafrost regions', *Remote Sensing*, vol. 9, no. 7, p. 640, 2017.

[3] T. Tarasenko, 'Interannual variations in the areas of thermokarst lakes in central yakutia', *Water Resources*, vol. 40, no. 2, pp. 111–119, 2013.

[4] M. Previdi, K. L. Smith and L. M. Polvani, 'Arctic amplification of climate change: A review of underlying mechanisms', *Environmental Research Letters*, 2021.

[5] E. A. Schuur, A. D. McGuire, C. Schädel, G. Grosse, J. W. Harden, D. J. Hayes, G. Hugelius, C. D. Koven, P. Kuhry, D. M. Lawrence *et al.*, 'Climate change and the permafrost carbon feedback', *Nature*, vol. 520, no. 7546, pp. 171–179, 2015.

[6] M. Ulrich, H. Matthes, L. Schirrmeister, J. Schütze, H Park, Y. Iijima and A. N. Fedorov, 'Differences in behavior and distribution of permafrost-related lakes in c entral y akutia and their response to climatic drivers', *Water Resources Research*, vol. 53, no. 2, pp. 1167–1188, 2017.

[7] J. Ramage, L. Jungsberg, S. Wang, S. Westermann, H. Lantuit and T. Heleniak, 'Population living on permafrost in the arctic', *Population and Environment*, vol. 43, no. 1, pp. 22–38, 2021.

[8] A. H. Lachenbruch, *Mechanics of thermal contraction cracks and ice-wedge polygons in permafrost*. Geological Society of America, 1962, vol. 70.

[9] R. F. Black and W. L. Barksdale, 'Oriented lakes of northern alaska', *The Journal of Geology*, vol. 57, no. 2, pp. 105–118, 1949.

[10] D. Derksen, K. Bollinger, D Esler, K. Jensen, E. Taylor, M. Miller and M. Weller, 'Effects of aircraft on behavior and ecology of molting black brant near teshekpuk lake, alaska', *OCS Study MMS*, pp. 92–0063, 1992.

[11] C. J. Markon and D. V. Derksen, 'Identification of tundra land cover near teshekpuk lake, alaska using spot satellite data', *Arctic*, pp. 222–231, 1994.

[12] M. Fuchs, G. Grosse, B. M. Jones, J. Strauss, C. A. Baughman and D. A. Walker, 'Sedimentary and geochemical characteristics of two small permafrost-dominated arctic river deltas in northern alaska', *arktos*, vol. 4, no. 1, pp. 1–18, 2018.

[13] K. Liu, W. Shi and H. Zhang, 'A fuzzy topology-based maximum likelihood classification', *ISPRS Journal of Photogrammetry and Remote Sensing*, vol. 66, no. 1, pp. 103–114, 2011.

[14] L. Bruzzone and L. Carlin, 'A multilevel context-based system for classification of very high spatial resolution images', *IEEE transactions on Geoscience and Remote Sensing*, vol. 44, no. 9, pp. 2587–2600, 2006.

[15] S.-S. Tseng, J.-M. Su, G.-J. Hwang, G.-H. Hwang, C.-C. Tsai and C.-J. Tsai, 'An object-oriented course framework for developing adaptive learning systems', *Journal of Educational Technology & Society*, vol. 11, no. 2, pp. 171–191, 2008.

[16] B. Jin, Y. Tang, Y.-Q. Zhang, C.-D. Lu and I Weber, 'Support vector machine with the fuzzy hybrid kernel for protein subcellular localization classification', in *The 14th IEEE International Conference on Fuzzy Systems, 2005. FUZZ'05.*, IEEE, 2005, pp. 420–423.

[17] L. Breiman, 'Random forests', *Machine learning*, vol. 45, no. 1, pp. 5–32, 2001.

[18] M. Immitzer, C. Atzberger and T. Koukal, 'Tree species classification with random forest using very high spatial resolution 8-band worldview-2 satellite data', *Remote sensing*, vol. 4, no. 9, pp. 2661–2693, 2012.

[19] A. W. Abbas, N Minallh, N. Ahmad, S. A. R. Abid and M. A. A. Khan, 'K-means and isodata clustering algorithms for landcover classification using remote sensing', *Sindh University Research Journal-SURJ (Science Series)*, vol. 48, no. 2, 2016.

[20] D. B. Goldman, 'Vignette and exposure calibration and compensation', *IEEE transactions on pattern analysis and machine intelligence*, vol. 32, no. 12, pp. 2276–2288, 2010.

[21] D. Lu and Q. Weng, 'A survey of image classification methods and techniques for improving classification performance', *International journal of Remote sensing*, vol. 28, no. 5, pp. 823–870, 2007.

[22] B. Usman, 'Satellite imagery land cover classification using k-means clustering algorithm computer vision for environmental information extraction', *Elixir International Journal of Computer Science and Engineering*, vol. 63, pp. 18 671–18 675, 2013.

[23] L. M. Abualigah, A. T. Khader and E. S. Hanandeh, 'A hybrid strategy for krill herd algorithm with harmony search algorithm to improve the data clustering', *Intelligent Decision Technologies*, vol. 12, no. 1, pp. 3–14, 2018.

[24] D. Comaniciu and P. Meer, 'Robust analysis of feature spaces: Color image segmentation', in *Proceedings of IEEE computer society conference on computer vision and pattern recognition*, IEEE, 1997, pp. 750–755.

[25] ——, 'Mean shift: A robust approach toward feature space analysis', *IEEE Transactions on pattern analysis and machine intelligence*, vol. 24, no. 5, pp. 603–619, 2002.

[26] K. Fukunaga and L. Hostetler, 'The estimation of the gradient of a density function, with applications in pattern recognition', *IEEE Transactions on information theory*, vol. 21, no. 1, pp. 32–40, 1975.

[27] J. N. Kaftan, A. A. Bell and T. Aach, 'Mean shift segmentation-evaluation of optimization techniques.', in *VISAPP (1)*, 2008, pp. 365–374.

[28] M. Belgiu and L. Drăguţ, 'Random forest in remote sensing: A review of applications and future directions', *ISPRS journal of photogrammetry and remote sensing*, vol. 114, pp. 24–31, 2016.

[29] M. Cámara and F. López, 'Mathematical morphology applied to raster generalization of urban city block maps', *Cartographica: The International Journal for Geographic Information and Geovisualization*, vol. 37, no. 1, pp. 33–48, 2000.

[30] G. Deng and L. Cahill, 'An adaptive gaussian filter for noise reduction and edge detection', in *1993 IEEE conference record nuclear science symposium and medical imaging conference*, IEEE, 1993, pp. 1615–1619.

[31] M. Roushdy, 'Comparative study of edge detection algorithms applying on the grayscale noisy image using morphological filter', *GVIP journal*, vol. 6, no. 4, pp. 17–23, 2006.

[32] R Congalton and K Green, *Accuracy assessment of remotely sensor data: Principles and practices*, 1998.

[33] Y. Liu, X. Zheng, G. Ai, Y. Zhang and Y. Zuo, 'Generating a high-precision true digital orthophoto map based on uav images', *ISPRS International Journal of Geo-Information*, vol. 7, no. 9, p. 333, 2018.